Shock interacting with a random array of stationary particles underwater

Jacob Behrendt [1], S. Balachandar [1], and T. P. McGrath [2]
[1] *Department of Mechanical and Aerospace Engineering (MAE), University of Florida, Gainesville, Florida 32611, USA*
[2] *Naval Surface Warfare Center, Indian Head Division, Indian Head, Maryland 20640, USA*

(Received 8 July 2021; accepted 27 January 2022; published 28 February 2022)

Accurately predicting the force experienced by particles within a random bed during shock traversal is a challenging problem. In this paper, particle-resolved inviscid simulations of shock propagation over randomly distributed beds are performed, with the goal of quantifying the force on individual particles. Water was considered the continuum material, and then results were compared with previous research completed in air and the differences resulting from these different mediums were examined. Simulations were conducted for four different combinations of incident Mach number and bed volume fraction with the particles remaining stationary. Time-resolved streamwise and transverse force coefficients were calculated for each particle in the bed. It was observed that while the average force coefficient was similar to that of an isolated particle, the force on individual particles was substantially different. An important observation was that the inviscid drag force on some particles remained consistently positive, but others consistently negative even long after the passage of the shock. This persistent force on the particle was attributed to the potential flow fields that result from neighbors' specific locations upstream and downstream. Similar behavior was observed in the transverse force, with particles experiencing sustained force in the same lateral direction. These persistent forces are inviscid quasisteady contributions which with the viscous counterpart will play an essential role in the particle's long-term dispersion if allowed to move in response to the force.

DOI: 10.1103/PhysRevFluids.7.023401

I. INTRODUCTION

The dynamics of a shock interacting with particles is a key feature in several industrial applications and occurrences in nature. For example, volcanic eruptions [1], drug delivery systems [2], and supernovas all consist of flows with shocks and multiple phases present. It is essential to understand the physical mechanisms that dictate the nature of these shocked multiphase flows. Numerous physical complexities exist, including compression waves, expansion fans, and small-scale turbulence. These features are significantly impacted by the arrangement of particles within the flow. The wide range of length and timescales present formidable challenges to creating models, performing numerical simulations, and analyzing physical experiments. Real systems may contain upwards of a billion particles in the flow. Fully resolving the flow around these particles in a numerical simulation is not currently possible.

Existing studies of shock-particle interaction can be broadly classified into three groups. The first group of studies focuses on shock-particle interaction at an isolated particle level. There has been a considerable amount of experimental, simulation, and modeling efforts focused on understanding the diffraction of the shock around the particle, with particular attention paid to the unsteady drag force on the particle during the passage of the shock [3–11]. The unsteady drag force was shown to be substantially larger than what would be predicted with a quasisteady drag model [9].

Particle-resolved simulation results and model predictions of compressible force [9–12] were in good agreement with the experimental results of [7]. Fedorov *et al.* [13] developed a mathematical model by processing experimental data on particle trajectories and velocities. In some cases, the heat transfer that occurs in a shock-particle interaction can play a noticeable role [14].

Single particle studies provided a foundational understanding. However, most real-life applications involve the interaction of a shock wave with a large distribution of particles. The second group of studies therefore considered, both experimentally and computationally, shock-induced dispersion of a cloud or a bed of particles [14–28]. Due to the large number of particles, the experiments focused only on the particles' collective behavior, such as the motion of upstream and downstream particulate fronts. Numerical simulations employed Euler-Lagrange (EL) or Euler-Euler (EE) methodologies. Flow around the particles was not resolved, leading to models being needed for the details of shock interaction with individual particles. The force models that couple the flow and the particulate phases are typically empirical extensions of those developed for an isolated particle. Of particular importance to the present discussion is the fact that these force models are statistically averaged in their formulation and depend on Reynolds number, Mach number, and volume fraction, evaluated at the mesoscale. As a result, these EL and EE simulations do not account for the full range of interactions among the particles. Based on recent particle-resolved simulations of steady incompressible flow over a random array of particles [29–34], it can be expected that gas-mediated interaction between the particles within a random array will lead to substantial particle-to-particle force variation, even when all the particles nominally "see" the same planar shock propagating over them. But such particle-to-particle force variation is ignored in the above EL and EE simulations.

The third group of investigations involves studies of shock propagation through a bed containing hundreds of particles. To study the effect of streamwise spacing between particles, Sridharan [35] studied the drag on a 1D chain of particles by systematically varying the spacing between the particles and the Mach number of the incident shock. Mehta *et al.* [36] and Hosseinzadeh-Nik *et al.* [37] both studied a transverse array of particles and reported fluid-mediated interaction between particles that can lead to higher than expected drag due to constructive wave interference. Mehta *et al.* [38] investigated shock propagation through a structured face-centered-cubic (FCC) array of particles for varying shock Mach numbers and particle volume fractions. This work revealed complex shock interactions within the bed, which led to significant modifications in fluid flow and particle drag. Shock interaction with a random distribution of stationary uniformly sized particles was considered in [39–42] to quantify the differences in the behavior of different static particle arrangements. The particle-resolved, three-dimensional, inviscid simulations of [40,41] with a random distribution of particles at various incident shock Mach numbers and volume fractions are of particular relevance to the present work. Those studies reported, within a random array, individual particle force histories are vastly different compared to those of an isolated particle.

The above three groups of studies can be characterized as microscale, macroscale, and mesoscale investigations. While the single and multiple particle-resolved studies were highly accurate, they do not scale easily to a full system consisting of millions to billions of particles, where one must resort to EL and EE approaches. However, the accuracy of macroscale EL and EE simulations depends critically on the force models' fidelity that couple the fluid and the particulate phases. It is thus essential to gain a better understanding of shock propagation over a bed of particles through particle-resolved simulations so that appropriate force models can be developed for use in future EL and EE simulations. We seek two levels of information from the particle-resolved simulations of shock-particle interaction. The first and basic information we seek is the average force on a random distribution of particles during their interaction with the shock wave. Since the pioneering work of Basset, Boussinesq, Oseen, Maxey and Riley, the unsteady conditions such as those encountered during shock passage, it is customary to separate the particle force into pressure-gradient, quasisteady, added-mass, and viscous unsteady contributions [43]. Among these, during the early period when the shock is located within a few diameters of the particles, inviscid forces (pressure-gradient and added-mass forces) dominate, which will be the focus of the present

study.[1] The next level of information we seek from the particle-resolved simulations pertains to the force on individual particles within the random array and how they depart from the average force. An accurate model of average shock-induced force on a layer of particles and how the force varies across the layer at the mesoscale is essential for predicting the mean motion of the layer and the stretching of the layer along the flow direction. Alternatively, accurate information on how the force varies from particle-to-particle is essential to predict the dispersal of particles.

The present work extends the prior research of shock interaction with a random particle bed reported in [40,41]. Those works used air as the working fluid, focused on early-time inviscid response, and assumed the particles to remain fixed and rigid over the time frame investigated. This work considers the analogous scenario in which water is the working fluid. In addition to being three orders of magnitude more dense than air, water is a considerably stiffer material, with an ambient sound velocity more than four times that of air. These factors result in significant modifications to shock-particle interaction, which are shown and contrasted with the air-shock results of [40,41]. The use of water as the medium offers a significant simplification of the flow analysis. The nature of the postshock flow within the random array depends on the Mach number of the postshock flow. For postshock Mach numbers greater than 0.6 (termed the critical Mach number), shocklets and bow shocks form around the individual particles, resulting in dissipation, and the strength of the incident shock weakens as it propagates through the bed. In the case of water, even at larger shock Mach numbers, the postshock flow remains subcritical, and the shock propagates through the bed of particles, maintaining its strength. As a result, in calculating the average and RMS force, all the particles within the bed, except for those within a thin layer at the leading and trailing fronts, can be used in obtaining the statistics since they "see" the same shock. With air as the medium, even a modest incident shock Mach number leads to a supercritical postshock flow. Since the shock strength weakens as it moves downstream, different particles depending on their streamwise location see different shock strengths and thus cannot be meaningfully averaged. Thus, in the case of water, we obtain better statistical information, which can be used to develop more accurate force models [29,44,45]. Furthermore, the observation of sustained positive and negative inviscid force on the particles in the postshock uniform flow is new since their extraction was considerably simplified due to the subcritical nature of the postshock flow in the case of water. Furthermore, it has been recently shown that the drag coefficient of an isolated particle subjected to water shock can be three times that when subjected to an air shock of the same strength [46], and is a result of differences in the equation of state. Therefore, it is of interest to see the effect of the equation of state in the case of shock propagation over a random distribution of particles.

In this work, we have also carried out a detailed investigation of the near-neighbor effects as a way to understand the mechanisms by which the force on individual particles is higher or lower than the average. This analysis has offered several important findings. First, while the average drag force on the bed is similar to that of a single particle, individual particle drag deviates considerably. The peak drag force differs, and a long-term quasisteady force, positive or negative, is observed. These deviations are a product of neighbor particle position, which creates wave refractions modifying the local trajectory of the incoming shock, reflections that lead to transient features in the drag history, and potential-flow effects that persist for all time. Second, while the average transverse force on the particle bed is zero, individual particles experience a significant deviation from the mean, with a nonzero quasisteady component that persists in time. These deviations arise for the same reasons as the streamwise force deviations. Furthermore, the deviations in peak drag and the persistent forces do not correlate to local Voronoi volume but are a function of local neighbor position. This finding is demonstrated through a simple one-dimensional array example which shows a direct functional dependence on proximity upstream and downstream of neighboring particles.

[1]Over a longer time, viscous effects become important, and their contribution can be added to the inviscid force.

The present investigation of inviscid flow over a random distribution of stationary particles is of intrinsic scientific interest in its own right. However, when it comes to applying the present results to EL and EE simulations of shock-induced motion and dispersion of a layer of particles, two important simplifications of the present investigation must be addressed. The first is the assumption that the particles are stationary, while in real applications particles are free to move. A timescale analysis of particle interaction with a water shock is presented in Sec. II B, where it is shown that the effect of particle motion is relatively small. The second approximation is the neglect of viscosity. Here again, the timescale analysis will show that viscous effects are minor during early times when the shock is only a few diameters downstream of the particle. However, the viscous contribution to force cannot be ignored at longer times.

The paper is organized as follows. The governing equations, numerical method, simulation setup, grid resolution, drag calculation, and averaging process are presented in Sec. II. In Sec. III the results of a single-particle simulation are first shown to demonstrate key differences between air and water. Following this, the results from random bed simulations performed using the shock Mach numbers and particle volume fractions previously considered by Mehta *et al.* [40,41] are presented. Then the streamwise force, transverse force, and properties of the flow are quantified, and the role of neighboring particles are examined. Last, conclusions are presented in Sec, IV.

II. MODEL DESCRIPTION

This paper investigates the interaction of a water shock with a bed of randomly distributed monodispersed spherical particles. The problem is studied at various shock Mach numbers and volume fractions. Following previous works [40,41], simulations are performed in the context of inviscid flow and fixed, rigid particles.

A. Governing equations and numerical methods

The applicable three-dimensional equations governing an inviscid fluid are the Euler equations

$$\frac{\partial \rho}{\partial t} + \nabla \cdot (\rho \mathbf{u}) = 0, \tag{1}$$

$$\frac{\partial (\rho \mathbf{u})}{\partial t} + \nabla \cdot (\rho \mathbf{u}\mathbf{u}) + \nabla p = 0, \tag{2}$$

$$\frac{\partial E}{\partial t} + \nabla \cdot ((E + p)\mathbf{u}) = 0, \tag{3}$$

where ρ is the density, $\mathbf{u} = (u,v,w)$ is the velocity vector, p is the pressure, and E is the total energy per unit volume, which is a function of the internal energy, e,

$$E = \rho\left(e + \tfrac{1}{2}\mathbf{u} \cdot \mathbf{u}\right). \tag{4}$$

Pressure is defined via the stiffened gas equation of state, which has been used by previous researchers to represent water [47–49]:

$$p = \rho e(\gamma - 1) - \gamma P^{\infty}. \tag{5}$$

Water is modeled using the constants $\gamma = 4.4$, $P^{\infty} = 0.6\,\text{GPa}$. Air is modeled using the ideal gas limit by setting $\gamma = 1.4$, $P^{\infty} = 0$.

The Euler equations are solved with a finite-volume solver on a body-conforming unstructured grid, which conforms to the particle surfaces. The fluid flow exterior to the spheres is discretized with a well-resolved unstructured grid. The fluxes are computed using a second-order accurate AUSM+ scheme [50]. The gradients are modified using a weighted essentially nonoscillatory (WENO) reconstruction technique [51]. A third-order Runga-Kutta method is used to carry out the time integration. This code has been tested and validated previously in several problems involving compressible flows with shock waves [9,23,52,55].

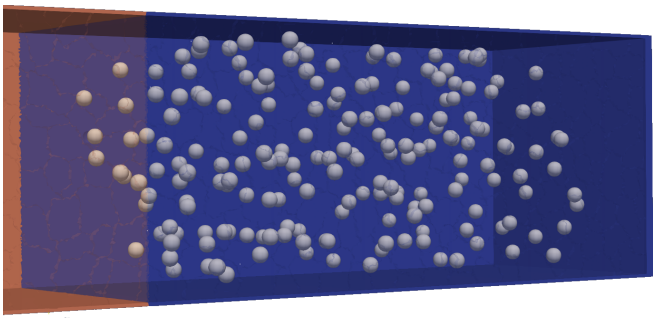

FIG. 1. 3D view of domain.

B. Simulation geometry and initial conditions

The simulation geometry consists of a random distribution of monodispersed particles inside a three-dimensional rectangular box. An example is shown in Fig. 1. The domain length is equal in the transverse (y and z) directions and longer in the streamwise (x) direction. The computational domain is initially separated into two distinct regions: (1) shocked water that is upstream of the incident primary shock and (2) quiescent, preshock ambient water that contains particles. The initial states are chosen such that a shock wave propagates to the right starting from the initial condition, with no other waves generated in the process. When the primary shock encounters the particles, multiple shock reflections occur. The nature of these reflected waves depends on the Mach number of the postshock flow. If the postshock Mach number is above the critical Mach number (about 0.6 for an isolated sphere in a uniform ambient flow), shocklets are expected to form as the flow accelerates around the particles. When the postshock Mach number is supersonic, the resulting reflections will form bow shocks ahead of the individual particles. When shocklets or bow shocks form in both of these regimes, the primary shock energy decreases as it moves through the bed.

The pressure, density, velocity, and temperature of the flow in the pre- and postshock regions of the flow are related by the Rankine-Hugoniot equations, which are well known for the ideal gas EOS and can be easily derived for the stiffened gas EOS. Here we are interested in the relation between the Mach number of the postshock flow and the shock Mach number. The equation for calculating the postshock Mach number, given the incident Mach number, is the same for ideal gas and stiffened gas, which is

$$M_2 = \frac{(\gamma+1)M_s^2}{\sqrt{\left[(\gamma+1)+2\gamma\left(M_s^2-1\right)\right]\left[2+(\gamma-1)M_s^2\right]}} - \sqrt{\frac{2+(\gamma-1)M_s^2}{2\gamma\left(M_s^2-1\right)+(\gamma+1)}}. \tag{6}$$

It is instructive to consider the different postshock Mach numbers generated for the well-studied case of air compared with those for water, which is the focus of the present study. Figure 2 compares the postshock Mach numbers for air (blue line) and water (red line) over a range of incident Mach numbers. The horizontal dashed black lines indicate the critical and supersonic Mach numbers. The vertical dashed black lines are the incident Mach numbers considered in this paper, 1.22 and 3. With increasing shock Mach number, the postshock Mach number saturates for both materials, but there is a stark difference in the postshock Mach numbers reached. For air the postshock Mach number becomes supercritical and supersonic for primary shock Mach numbers 1.50 and 2.07. The postshock Mach number remains subcritical for all primary shock Mach numbers considered for water.

As a consequence of the results shown in Fig. 2, we observed that for air, the postshock flow could support shocklets and bow shocks. The associated energy dissipation results in the progressive weakening of the primary shock even in inviscid simulations [40,41]. In contrast, for water, the

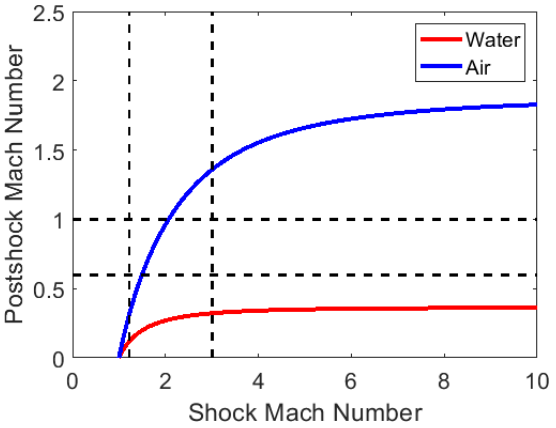

FIG. 2. Comparing the postshock Mach numbers of stiffened gas EOS for water vs the ideal gas EOS of air.

postshock flow remains subcritical; as a result, the primary shock maintains its intensity as it propagates through the bed of particles.

The setup of the inviscid simulations has two important length scales: the particle diameter and the mean spacing between the particles, which is related to the mean volume fraction of particles within the bed. The computational domain extends over 26 particle diameters in the streamwise direction, while the particle bed extends over 17 particle diameters. Thus, the computational domain includes an upstream length of nine particle diameters without particles. Here we set $x = 0$ at the particle bed center, and the particle bed extends from $x = -8.5d_p$ to $x = 8.5d_p$. In the transverse directions the computational domain extends from $y, z = -4d_p$ to $4d_p$. The particles are randomly distributed with a uniform probability that they entirely lie within the cuboidal region of size $17d_p \times 8d_p \times 8d_p$, which will be defined as the *particle bed*. The mean volume fraction ϕ is defined as the ratio of particle volume to the volume of the cuboidal region

$$\phi = \frac{\text{volume of particles}}{\text{volume of bed}}. \tag{7}$$

The simulations were performed until the primary shock reaches the downstream boundary of the bed, and the upstream length is sufficient to ensure that the reflection from the particle bed does not reach the upstream boundary in the simulation time frame. Thus, the upstream boundary is considered a constant inflow plane with properties equal to the postshock flow. More information on the computational domain can be seen in Table I, where x_{part} is the length of the particle bed and x_{upstream} is the distance between the inflow boundary and start of the particle bed. All other boundaries, including the transverse walls and the particle surfaces, are treated as slip walls.

Four cases were considered, with incident shock Mach numbers of $M_s = 1.22$ and 3.0 and volume fractions of 10% and 20%. The preshock state is quiescent ambient water with $p = 101{,}325$ Pa and $\rho = 998.0$ kg/m^3. Table II gives details of each case, including the postshock conditions. The naming convention denotes low and high Mach cases as LM and HM, wsith the volume fraction appended afterward. The postshock pressure is above the yield stress for many materials, indicating

TABLE I. Computational domain details with particle volume fraction.

ϕ	d_p (μm)	N_p	x_{part}/d_p	x_{upstream}/d_p	$(y, z)/d_p$
10%	100	200	17	9	8
20%	100	400	17	9	8

TABLE II. Values for primary shock Mach number M_s; postshock pressure p_{ps}; postshock density ρ_{ps}; postshock velocity u_{ps}; postshock Mach number $M_{ps} = u_{ps}/c_{ps}$, where c_{ps} is the postshock speed of sound; shock velocity u_s; and transit time $\tau = d_p/u_s$.

Case	M_s	ϕ	p_{ps} (MPa)	ρ_{ps} (kg/m^3)	u_{ps} (m/s)	M_{ps}	u_s (m/s)	τ (ns)
LM10	1.22	10%	477.73	1136.1	241.2	0.118	1984.4	50.39
LM20	1.22	20%	477.73	1136.1	241.2	0.118	1984.4	50.39
HM10	3.0	10%	7823.7	1487.8	1606.5	0.322	4879.7	20.49
HM20	3.0	20%	7823.7	1487.8	1606.5	0.322	4879.7	20.49

that deformation may occur. However, we evaluate the shock-particle interaction in the limit of rigid, spherical, and stationary particles in this work.

Five different timescales of relevance in shock-particle interaction problems were discussed by Mehta *et al.* [38]: (1) shock interaction time defined as the time it takes for the shock to cross a stationary particle given by $\tau_s = d_p/u_s$; (2) acoustic timescale defined as the time it takes for the acoustic wave to cross a stationary particle given by $\tau_a = d_p/c$, where c is the speed of sound in the quiescent medium; (3) inviscid timescale of postshock flow given by $\tau_i = d_p/u_{ps}$; (4) viscous timescale given by $\tau_v = \delta_v^2/\nu$, where δ_v is the viscous boundary layer thickness; and (5) particle timescale given by $\tau_p = \rho d_p^2/18\nu$, where ρ is particle-to-fluid density ratio and ν is fluid viscosity [38,55]. The particle timescale is the timescale on which the particle moves in response to forces acting on it. If we consider steel particles of radius 100 μm subjected to a low or high intensity shock listed in Table II, the ratio of particle to shock interaction timescale can be evaluated as $\tau_p/\tau_s = 10^4$ and 7×10^4, respectively. These values are somewhat lower than those for particles in air shock due to the lower particle-to-fluid density ratio. Nevertheless, the large value of τ_p/τ_s indicates that the downstream motion of particles is on a much slower timescale. Recent particle resolved simulations [46] of an isolated particle subjected to a planar shock in water confirm this scaling by observing that the particle force remains nearly the same whether the particle remains stationary or allowed to move freely, since the motion of the particle is quite slow during the period of shock interaction.

The importance of viscous effects can similarly be evaluated through the ratio τ_v/τ_s. For 100 μm particles in water, this ratio takes the values of 8 and 3 at the low and high Mach numbers, respectively. These ratios are not very large, and therefore viscous effects become important not long after the passage of the shock [41,53,54]. Inviscid forces, however, dominate at the early time. For example, the peak force on the particle (which happens when the shock is slightly downstream of the particle center) is dictated primarily by inertial effects and unaffected by viscosity. Thus, the force on the particles after the shock has moved several diameters downstream will be influenced by viscosity. Therefore, the present inviscid simulations will provide valuable information only on the inviscid component of the postshock flow on the particles. This inviscid contribution for a random distribution of particles has hitherto been not studied.

C. Grid resolution

The computational domain was discretized with an unstructured tetrahedral mesh. To generate the mesh on the sphere's surface, DistMesh [56] was used. After this step was completed, TetGen [57] was utilized to create the body-conforming unstructured tetrahedral mesh for the simulation domain. Support for the adequacy of resolution for shock propagation over the random distribution of particles tested comes from simulations of shock propagation over a face-centered cubic (FCC) array of particles [38]. In their simulations, Mehta *et al.* had a goal of maintaining a sharp shock and accuracy of the solution. The two factors that determine the sharpness of a shock and solution accuracy are the quality and size of the elements. It is necessary to have adequate resolution on the particle because the force is calculated by integrating flow properties on its surface. Furthermore, the element aspect ratio and maximum element volume control the quality and size of each element.

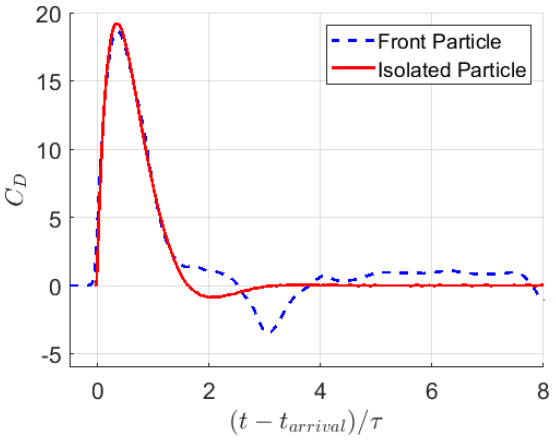

FIG. 3. Plot of drag for front particle in bed LM10 (dashed blue) and refined isolated particle (red) at the same Mach number.

In the study, they simulated a Mach 1.5 shock traversing through an FCC array of particles while varying the surface mesh per particle from 43 000 to 110 000 elements and total volume mesh from 6×10^6 to 30×10^6 elements. There were 25 different grids studied, and relative error in the drag at three different time instances was calculated for one of the particles. Overall, the optimal size of volume elements and surface mesh resolution required for accurate simulation of the incident shock and its propagation around the particles were determined. The optimal cell count for the grid that yielded the best balance between numerical accuracy and computation cost was chosen based on the relative error. Furthermore, the mesh resolution required for convergence was discussed in the case of a random array of particles for the ideal gas EOS [40].

The present study of shock propagation in water over a random distribution of particles maintained the same resolution level and satisfied all the conditions for convergence discussed in these references. To ensure the adequacy of resolution in the present context of stiffened gas EOS, we compared the drag coefficient of a well-resolved simulation of an isolated particles with the drag coefficient of the frontmost particle of the LM10 simulation. The comparison is shown in Fig. 3, where the dashed line of the front particle is in good agreement with the red line representing the isolated particle in capturing the initial rise, the peak, and the subsequent decay. As can be expected, at later times, the two results deviate due to the interaction with the neighboring particles in the case of LM10. The main takeaway is that the peak force is different by less than 3% proving the grid refinement validation applies to the current simulations.

D. Drag

Calculation of the drag coefficient on each particle in the flow is central to our analysis process. The drag coefficient is defined by

$$\mathbf{C}_D = \frac{\mathbf{F}}{\frac{1}{2}\rho_{ps} u_{ps}^2 A}, \tag{8}$$

where $\mathbf{F}$ is the force, ρ_{ps} is the postshock density, u_{ps} is the streamwise postshock velocity of the undisturbed flow, and $A = \pi d_p^2/4$ is the projected area of the particle with d_p equal to the particle diameter. Since the simulations are inviscid, the only contribution to force is from pressure distribution. The force can then be written as

$$F_i = \mathbf{F} \cdot \hat{e}_i \equiv \int_{S_p} p\hat{n} \cdot \hat{e}_i \, dS, \tag{9}$$

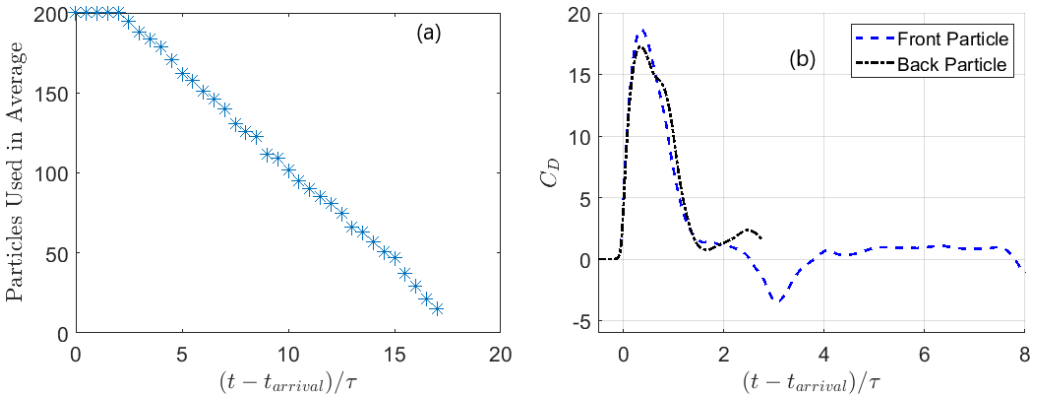

FIG. 4. (a) Number particles used for time averaging at different times for 10% volume fraction bed. (b) Drag for a particle in front and back of the bed to compare the time histories of the drag.

where $\hat{e}_i$ is the unit vector in the x_i direction, $\hat{n}$ is the outward normal, and S_p is the surface of the particle. From this definition, the drag coefficients in the x, y, and z directions are given by

$$C_D = \frac{F_x}{\frac{1}{2}\rho_{ps}u_{ps}^2 A}, \quad C_{D,y} = \frac{F_y}{\frac{1}{2}\rho_{ps}u_{ps}^2 A}, \quad C_{D,z} = \frac{F_z}{\frac{1}{2}\rho_{ps}u_{ps}^2 A}. \tag{10}$$

The total drag coefficient is calculated as $C_{D,T}^2 = C_D^2 + C_{D,y}^2 + C_{D,z}^2$.

E. Particle bed averaging

Bed averages can be calculated and compared with the single particle case to determine similarities and differences. The first step to calculate the average was to define the arrival time (t_{arrival}) for each particle. For this work, the arrival time is set as when the nondimensional streamwise drag becomes greater than 0.1. Arrival time is used to align the drag or impulse curves for all particles. The bed average values are computed by summation of drag or impulse, divided by the number of particles with time histories at that point. The number of particles used in the average varied over time. For example, the equation used to calculate the mean drag is

$$\overline{C_D}(t) = \frac{\sum_{i=1}^{N} C_{D,i}(t)}{N}, \tag{11}$$

where N is the total number of particles with time histories that extend to time t and $C_{D,i}$ is the drag value for the individual particle. Figure 4(a) shows the number of particles used for averaging at different dimensionless times for the 10% volume fraction cases; note that the shock transit time is defined as $\tau = d_p/u_s$. Additionally, the drag curves are shifted by the arrival time of the shock to the particle surface. Resulting in longer time histories for the particles near the front of the bed because they interact with the shock first. The particles in the back of the bed have shorter time histories because the simulation is stopped once the incident shock hits the downstream boundary. As a result, the early time averages are the most reliable due to more particles in the averaging process. To clarify this point, Fig. 4(b) compares the drag curves of two particles in the bed, one near the front and one near the back. This plot shows the drag curve on the front particle, dashed blue line, existing longer than the particle near the back of the bed, dashed-dot black line. The front particle will be a part of the averaging process for longer than the back particle. All the simulations ran a sufficient time for all particles to reach a peak drag value. A finite number of data points will always lead to some statistical uncertainty no matter the time. There is a significant particle-to-particle variation, but calculating the mean allows us to view the overall impact on the bed of particles.

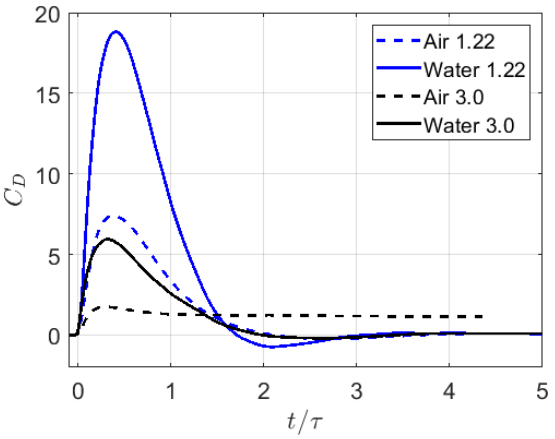

FIG. 5. Plot of drag for single-particle case for various Mach numbers and fluid media.

III. RESULTS

This section presents results and analysis from the shock-particle interaction scenarios defined in Table II. A short section comparing single-particle shock interactions in water vs air is presented as a precursor to this. That section highlights important differences stemming from the different fluid media and provides background that is referred to in later analysis. Following this, attention focuses on the shock-particle bed interaction problem in water. Results relating to streamwise and transverse forces are presented. The fluid flow-fields are examined to understand the forces better, and the effects of neighboring particles are analyzed.

A. Single particle air vs water

First, consider the simple case of a planar shock in either air or water transiting over a single particle. The computed drag coefficient is shown in Fig. 5 for both air (ideal gas EOS) and water (stiffened EOS) at shock Mach numbers of 1.22 and 3.0. Air and water produce substantially different results even in the limit of an isolated particle. The peak C_D in the case of air are 7.40 and 1.77 at $M_s = 1.22$ and 3.0, and these values are in excellent agreement with those reported in [7]. The peak C_D values in the case of water are 19.2 and 5.95 at the two Mach numbers, which are substantially larger than those of air. The time to peak drag decreases slightly with increased Mach number. It is also important to note that the long-time C_D is nonzero only for air at $M_s = 3.0$ since the supersonic postshock Mach number of 1.36 supports a reflected shock wave that quickly organizes to form a stationary bow shock ahead of the particle. The corresponding $M_s = 3.0$ water shock yields a postshock flow of Mach number 0.322, and therefore the inviscid drag force on the particle relaxes to zero after the passage of the primary shock. An incident shock Mach number of 1.22 yields a subcritical response for air and water. A negative C_D phase is observed at the lower Mach number for both materials, and water at $M_s = 3.0$, although in the latter case, it is of small magnitude. A closer inspection reveals the negative drag force for the $M_s = 3.0$ water-shock case is due to the focusing of the compressional wave on the rear side of the particle [58]. It is significant to note that these results show that the effect of numerical dissipation is quite negligible and does not have an impact on particle force. The steady state solutions for air $M_s = 1.22$, water $M_s = 1.22$, and water $M_s = 3.0$ all have zero drag. If numerical dissipation did influence these simulations, the long-time force would be nonzero. This result is also consistent with the numerical dissipative property of the AUSM+ scheme used in the present simulations (see [50]).

An important observation from this single-particle study is that a shock propagating through water produces a subcritical flow around the particle even for $M_s = 3.0$. This behavior is unlike the

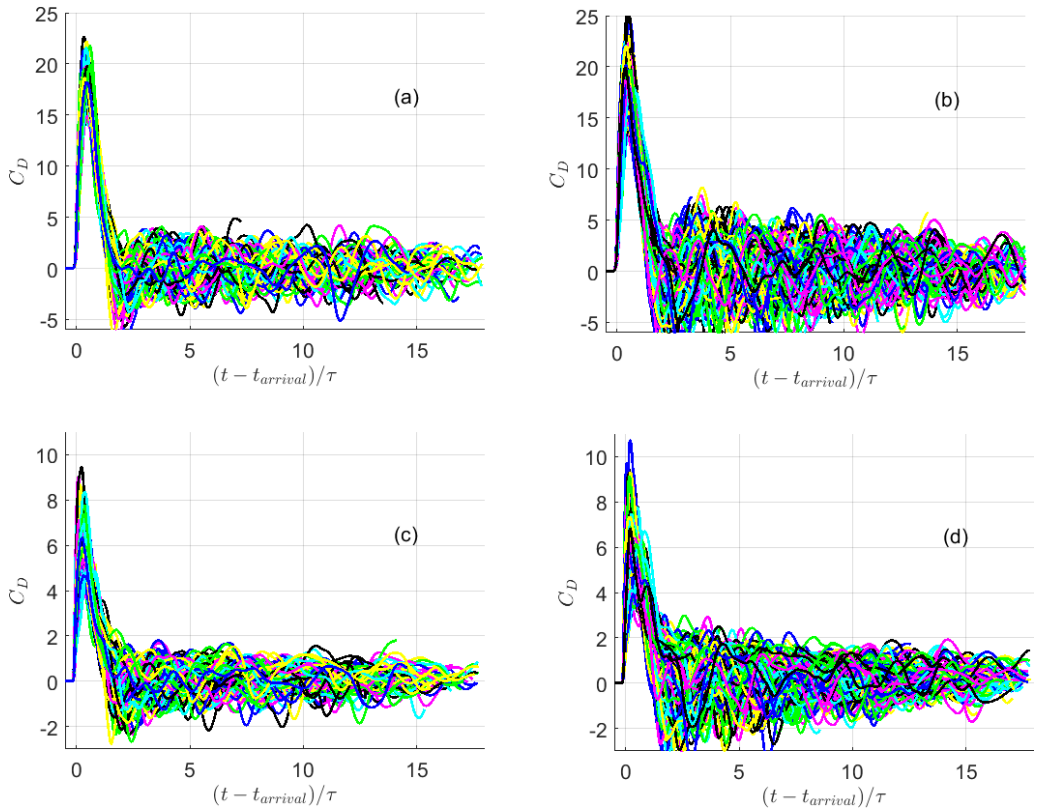

FIG. 6. Plot of C_D, streamwise drag coefficient, as a function of shifted nondimensional time $(t - t_{\text{arrival}})/\tau$. (a) LM10, (b) LM20, (c) HM10, (d) HM20.

case of air, where the supersonic postshock flow led to bow shock formation and the generation of a nonzero drag after the shock has passed. Instead, both the low and high Mach numbers lead to zero long-time drag in water for these inviscid simulations as a result of D'Alembert's paradox [59]. This observation will be contrasted with results obtained in particle-bed studies presented in Secs. III B and III C.

B. Streamwise force on the particles

Streamwise force histories, normalized as the drag coefficient, are shown in Fig. 6 for the four cases defined in Table II. These figures contain individual line plots representing the drag coefficient for each particle. The histories are shifted by the shock arrival time (t_{arrival}) for each particle and normalized by the transit time (τ). The resulting dimensionless time is: $\bar{t} = (t - t_{\text{arrival}})/\tau$. The plots show that all particles experience a rapid increase in drag force, with the peak being reached in less than half a shock transit time. The particles' drag force rapidly decreases after the peak and fluctuates near zero. The peak C_D, the decay rate, and the subsequent fluctuations vary substantially from particle to particle. These variations arise from positional variations in the random array. A unique distribution of neighbors surrounds each particle, and the flow perturbations induced by these neighbors are such that the time evolution of C_D is distinct. The long-time drag force on a particle is likely to be nonzero due to pressure fields produced by neighboring particles in the flow field.

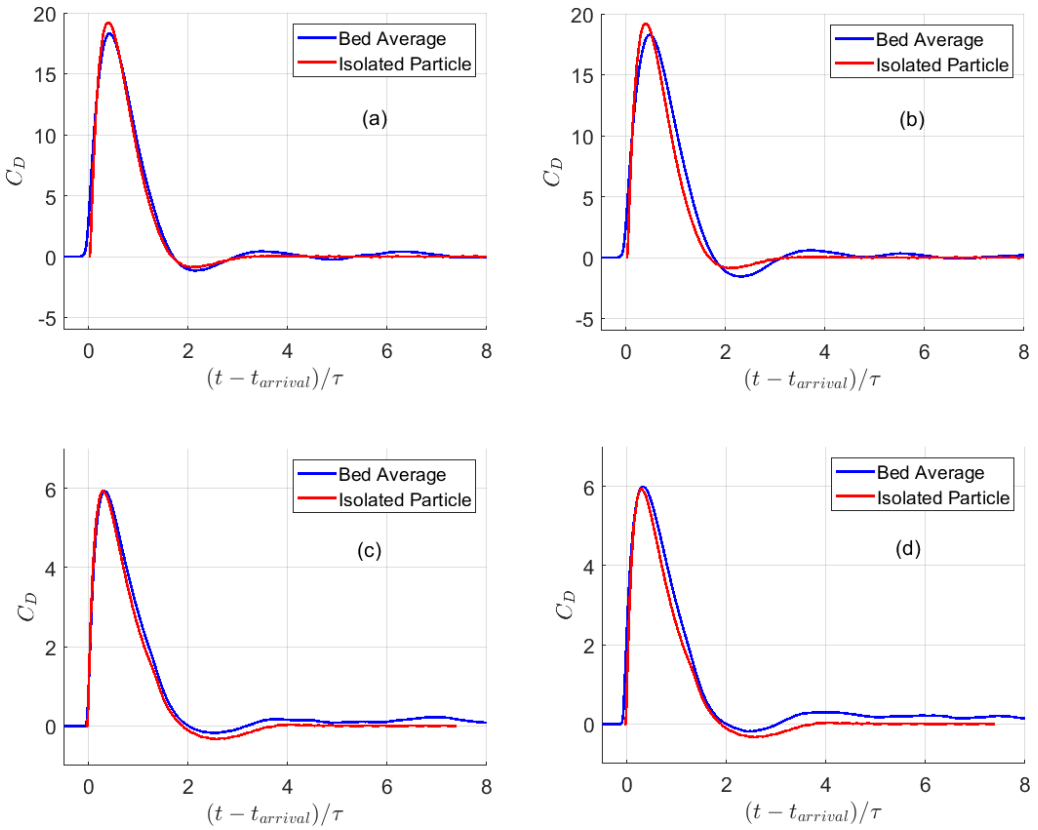

FIG. 7. Comparing average particle drag (blue) to isolated particle drag (red) as a function of shifted nondimensional time $(t - t_{\text{arrival}})/\tau$. (a) LM10, (b) LM20, (c) HM10, (d) HM20.

Figure 7 compares the drag coefficient time history for an isolated particle (red line) with the average C_D for the random pack (blue line). The time histories are qualitatively quite similar, but several observations can be made. For the low Mach number cases shown in Figs. 7(a) and 7(b), the bed-averaged peak drag coefficient is slightly lower than that of the single particle, and the rise time to the peak is slightly longer. For the high Mach number cases in Figs. 7(c) and 7(d), bed-averaged peak C_D and rise times are nearly identical to the single-particle result. From these results, it appears that the rise time and peak C_D are more closely correlated with Mach number, while the initial pulse duration is correlated with bed volume fraction. While Fig. 6 showed large oscillations persisting to late times, the bed-average results display only minor oscillations around zero, in agreement with the isolated particle results.

Overall, it is notable that given the variability in peak C_D and the subsequent large oscillations observed for individual particles shown in Fig. 6, the bed-averaged C_D is quite similar to the corresponding single particle C_D. This result is useful since it indicates that the mean drag of a random array during interaction with a planar shock can be well approximated by the drag of an isolated particle. This implies that the volume fraction of the random distribution does not play a major role during the early time of shock-particle interaction, as far as the average drag is concerned. However, the volume fraction plays an important role in determining the level of particle-to-particle variation about the average drag.

Another important consequence of the subcritical postshock flow is that the primary shock's strength remains the same over the entire time as it travels through the bed. Figure 8 shows this

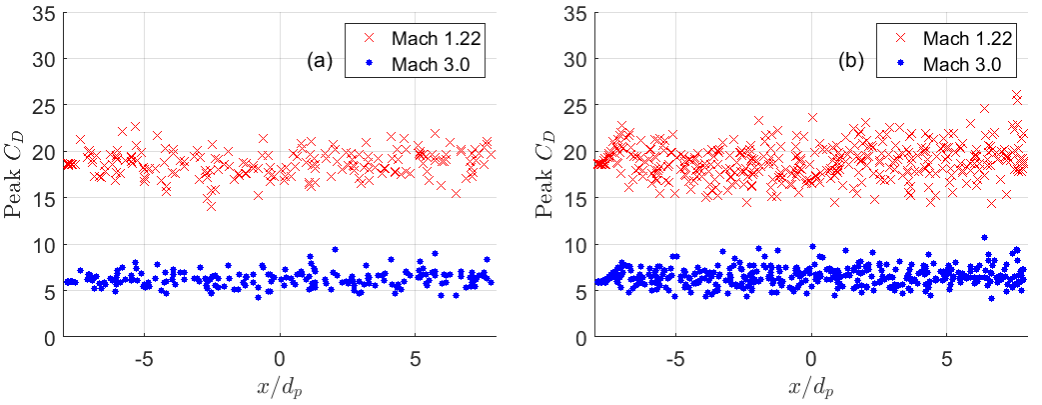

FIG. 8. Plot of peak C_D, streamwise drag coefficient, as a function of nondimensional streamwise position x/d_p. (a) $M_s = 1.22$ 10% VF (red), $M_s = 3.0$ 10% VF (blue),(b) $M_s = 1.22$ 20% VF (red), $M_s = 3.0$ 20% VF (blue).

behavior where the peak value C_D for all the particles within the bed are plotted as a function of the streamwise location of the particle center. The peak C_D does not diminish as the shock traverses the bed. Peak C_D varies due to constructive or destructive interference created by neighboring particles, but the average remains constant. The observed streamwise independence away from the leading and trailing particle fronts is absent in the air-shock cases studied by [25,40,60], where the shock strength monotonically decayed as it traveled through the bed, especially at $M_s = 3.0$. As a result, the peak forces at the downstream end of the bed were substantially lower than those at the bed's upstream end. In Table III we present the average and RMS values of the peak C_D computed for the entire bed for the four different cases. Generally, the average and the RMS peak values decrease with increasing shock Mach number and increase with volume fraction.

1. Streamwise impulse variation

An important question regarding the long-time force on individual particles remains unclear from the time histories of C_D shown in Fig. 6. From Fig. 7 it is clear that C_D when averaged over all the particles is zero (or nearly so, with a slight offset due to finite resolution and sample size).The time-averaged force on the individual particles is also of interest. The large oscillations in the individual particle histories shown in Fig. 6 make it challenging to assess whether forces persist on the particles or if C_D is oscillating around zero. To better visualize this, the nondimensional impulse defined as

$$I(t) = \int_{-\infty}^{t} C_D(t')\, dt' \tag{12}$$

is computed for each particle within the bed and plotted as a function of shifted nondimensional time in Fig. 9. Added in each plot is a red line that represents the bed average. An initial, rapid increase in impulse as the primary shock passes over each particle is present. It is the later-time results, occurring after initial shock passage ($\bar{t} > 2$), that are of most interest. Rather than rising to

TABLE III. Average and RMS values for peak streamwise drag.

	LM10	LM20	HM10	HM20
Average	18.67	18.91	6.21	6.53
RMS	1.41	1.87	0.85	1.00

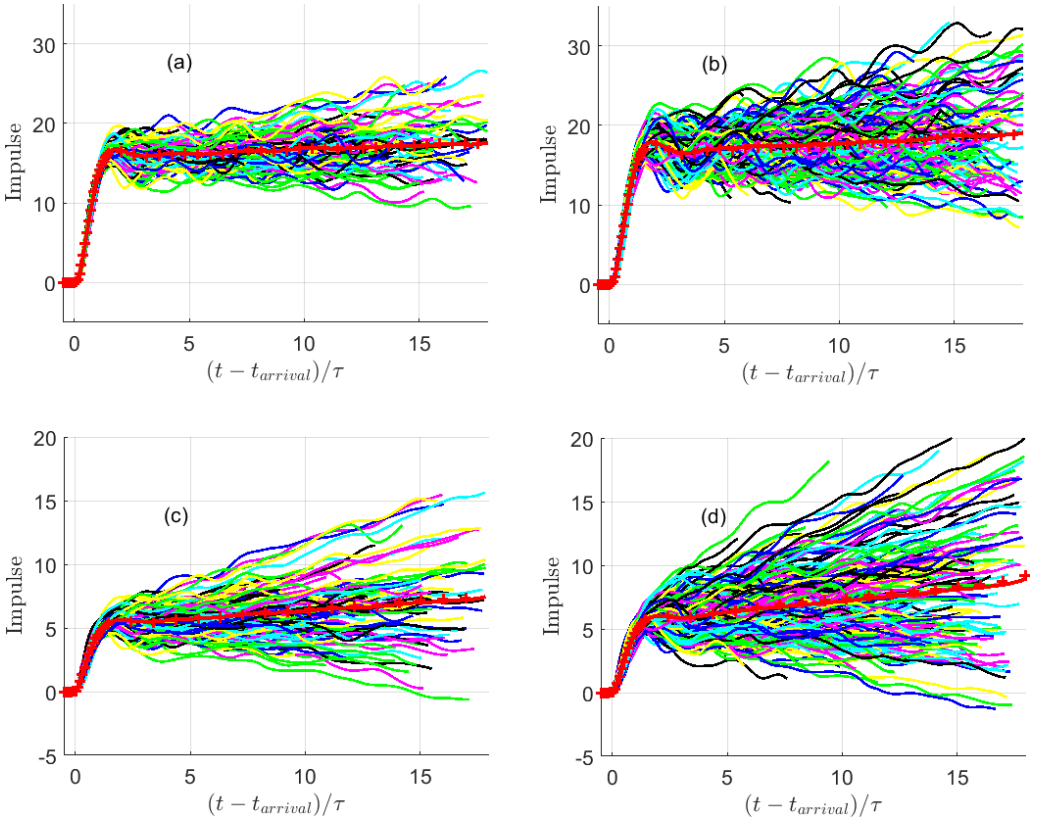

FIG. 9. Plot of impulse as a function of shifted nondimensional time $(t - t_{\text{arrival}})/\tau$. (a) LM10, (b) LM20, (c) HM10, (d) HM20.

different levels, dictated by the impulse delivered through the initial pulse and flattening out, the impulse retains a persistent positive or negative slope throughout the simulation. Thus, a nonzero average drag force persists on individual particles. Moreover, while there are oscillations in each line, the average slopes appear constant, indicating that the average net force on a given particle does not trend toward zero over time. Examining Fig. 9 in more detail, it can be noted that, consistent with the observation of a nonzero average late-time drag force in Fig. 6, the bed-average impulse (denoted by the red line) retains a small nonzero slope.

The slopes of the impulse-vs-time curves do not have a systematic dependence on the position of the particles within the bed. Instead, the value of the slope depends on the arrangement of upstream and downstream neighbors. The particle's position within the bed matters in deciding the length of time duration of the impulse curve for that particle. If the particle is closer to the upstream front, the impulse curve is available for a longer duration. Whereas, if the particle is located close to the trailing front, the impulse curve stops at a shorter time. Thus, the sample size over which the average is computed decreases as $(t - t_{\text{arrival}})$ increases. To eliminate the possibility of unwanted statistical bias due to varying sample size, the average was also computed only for those particles for which the data was available for the period $0 \leqslant (t - t_{\text{arrival}}) \leqslant 12$. This analysis allowed calculation of the impulse using a fixed number of 82 particles in the 10% volume fraction cases and 161 particles in the 20% volume fraction cases. The results obtained are also shown in Fig. 9 as red symbols. The difference between the red lines and symbols is relatively small, indicating sufficient statistical convergence of the results.

The temporal oscillations seen in the drag plots can also be observed in the time history of impulse. These oscillations are due to neighboring particles creating compression and rarefaction waves that then reflect off other particles causing secondary interactions, and so on. Due to constructive and destructive interference of these multiple compression and rarefaction waves, the pressure field around each particle varies over time. When the pressure in the wake region of a particle increases more than in front, a lower drag occurs. If the pressure variation is reversed, it creates a temporal increase of the drag on such a particle.

A careful investigation of the flow field (to be discussed in Sec. III D) shows that as the primary shock propagates through the bed of particles, the reflected waves from the primary shock front propagate backward. These waves diffract around the bed of particles, creating force fluctuations on the different particles. As the primary shock moves farther into the bed of particles, the strength of the reflected waves reaching the upstream particles diminishes, which explains the reduced amplitude of force fluctuation seen in Fig. 6. The random nature of temporal variation in drag shows that the neighboring particles perturb the wave interactions that propagate through the bed in a complex manner.

The persistent streamwise force on the individual particles can be identified as a steady increase or decrease of their impulse. The magnitude and direction (positive or negative) of the force for a given particle result from its position with respect to its neighbors within the bed. From the slope of the impulse plots, it can be inferred that the sustained drag force on the particles in the postshock flow is of substantial magnitude. For example, in the case of 20% volume fraction and Mach 3 shock, the sustained value of drag coefficient ranges between -0.5 to 1. Although smaller than the peak C_D value of about 6, the sustained drag coefficient is quite comparable to the standard drag coefficient of a sphere. It is also interesting to note that D'Alembert's paradox of zero inviscid drag applies only for the average drag of the entire cluster; that is, when averaged over all the particles within the distribution, the positive and negative forces nearly balance. However, individual particles within the cluster experience substantial positive or negative drag in the inviscid or potential limit. The perturbation flow fields of neighboring particles are the primary reason the individual particles' force does not decay but instead shows persistent nonzero behavior. Further discussion on the flow fields surrounding the particles is found in Sec. III E.

From a modeling perspective, the persistent inviscid force must be treated as a quasisteady contribution and considered along with the corresponding viscous contribution. The net long-term effect of the constant positive or negative force is substantial. For example, in the $M_s = 3$ case, it can be observed that the impulse on some of the particles due to the later-time persistent quasisteady-inviscid contribution during the interval $1 \lessapprox \bar{t} < 18$ is nearly two to three times the impulse deposited on the particle due to the initial shock interaction represented by the first peak. It can be seen that the net impulse becomes negative for some particles implying that for these particles, the initial impulse of the primary shock has been erased by the postshock inviscid flow. Of course, with viscous contribution, all particles within the array are expected to experience a net positive force that moves them downstream. Nevertheless, the effect of sustained positive or negative inviscid contribution highlights the importance of strong particle-to-particle force variation.

As the shock moves farther downstream from a particle, the effect of the reflected waves that emanate from the propagating primary shock can be expected to decay over time. Accordingly, the up-and-down oscillations of the impulse curve will diminish as well, and the impulse curve will take a persistent positive or negative slope. It must be cautioned that when particles are allowed to move in response to the hydrodynamic force in real systems, the relative positioning of particles will change in response to the net force acting on them. Under such conditions of nonstationary particles, the above observation of persistent positive or negative inviscid force is time evolving, both due to continuous changes in the neighborhood arrangement that is responsible for constructive or destructive interference and because the acceleration of the neighboring particles will also contribute to added-mass force on the particles [61].

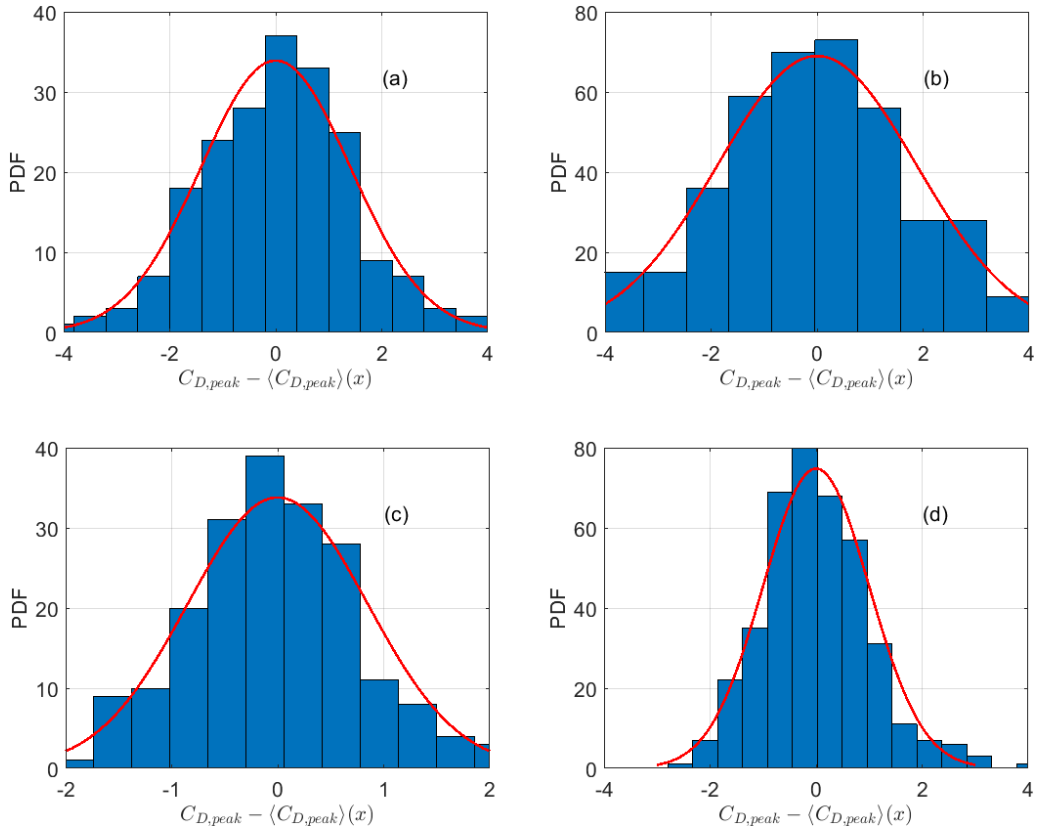

FIG. 10. Histogram plot of peak C_D, streamwise drag coefficient. (a) LM10, (b) LM20, (c) HM10, (d) HM20.

2. Peak drag statistics

To further quantify the peak drag, a histogram of $C_{D,\text{peak}} - \langle C_{D,\text{peak}} \rangle$ is shown in Fig. 10, where $C_{D,\text{peak}}$ is the individual peak of a particle and $\langle C_{D,\text{peak}} \rangle$ is the mean peak drag of the entire bed. The histograms are obtained by sorting the peak drag values into bins of equal width for each volume fraction. A red line that fits a normal distribution is plotted on each subfigure for comparison. In all cases, the distribution closely follows a normal distribution. It is clear that a point-particle drag model that yields the same drag force for all the particles within the random array, since they see the same macroscale primary shock, does not capture the physics of substantial particle-to-particle variation. Following the near-Gaussian distribution, a stochastic model based on Langevin model [29,62,63] can be formulated to capture the drag variation within the bed in a statistical sense, although such a stochastic model may not assign high and low drag to the correct particles.

The flow seen by each particle is unique and dependent on the precise location of the neighbors. The peak drag and the impulse on a particle directly result from relative positions of the upstream and downstream neighbors. One simple measure of neighbor particles is the Voronoi volume associated with each particle. A plot of the peak drag as a function of scaled Voronoi volume is shown in Fig. 11. In the figure, $\langle C_{D,\text{peak}} \rangle$ is the average peak drag value for all particles. Further, the scaled Voronoi volume is defined as $(\phi_V - \langle \phi_V \rangle)/\langle \phi_V \rangle$, where ϕ_V is the local Voronoi-based volume fraction of a particle calculated as the ratio of particle volume to its Voronoi volume that depends on the relative position of its neighbors. In the above, $\langle \phi_V \rangle$ is the Voronoi-based volume fraction averaged over the entire bed. A positive value of scaled Voronoi-based volume fraction

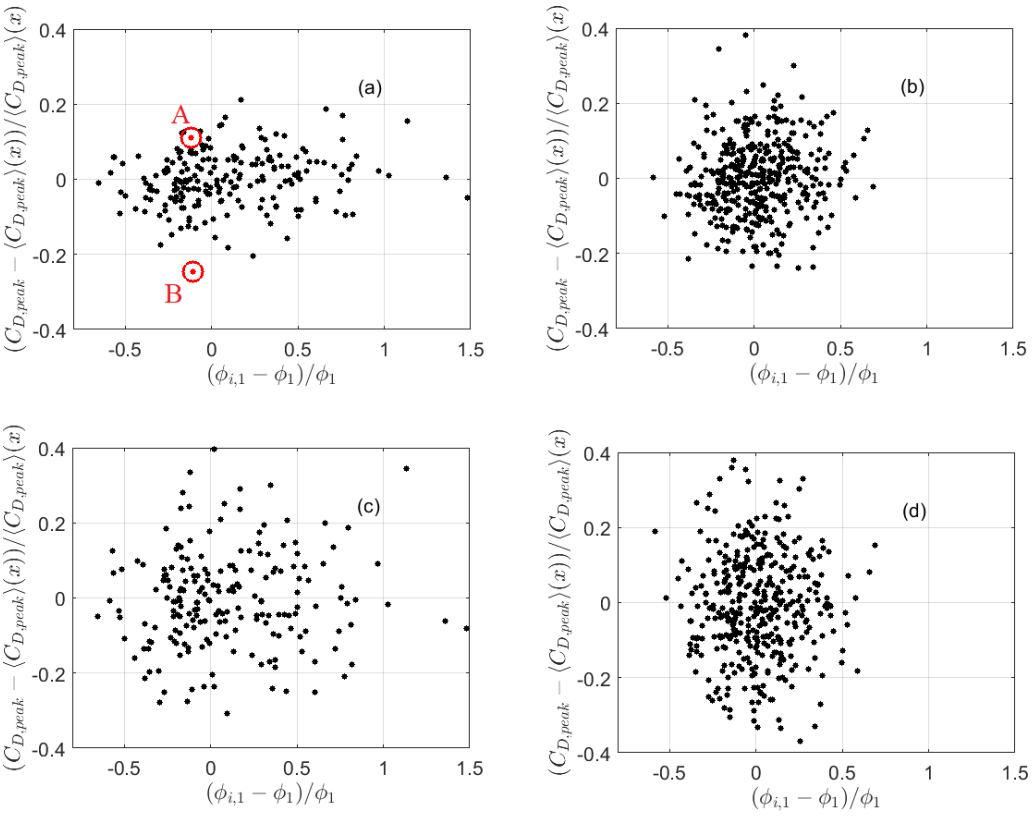

FIG. 11. Plot of normalized peak C_D, streamwise drag coefficient as a function of scaled local volume fraction. (a) LM10, (b) LM20, (c) HM10, (d) HM20.

corresponds to a particle being closely surrounded by its neighbors. Meanwhile, a particle with a significant negative value has a larger free space area around it. The 10% volume fraction plots are more spread out along the horizontal axis than the higher volume fraction cases. This packing is a result of there being less space between particles when the volume fraction is increased. Also, there is a more significant variation in the peak drag values with increasing volume fractions. The general lack of correlation between Voronoi-based volume fraction and drag has also been observed by [62] in the context of a uniform steady incompressible flow over a random bed of particles, where the deviation of drag force from the bed average does not correlate with the local volume fraction. Different definitions of local volume fraction, such as distance to the n-nearest neighbors [64,65] or number of particles within a reference volume [66], can be used instead to obtain a different measure of neighborhood rather than Voronoi volume. Even with the different definitions of local volume fraction, we cannot correlate particle-to-particle force variations in terms of local volume fraction [62]. An important downside of all such scalar measures of particle volume fraction is that they do not consider whether the neighbors are upstream or downstream of the particle. For instance, two particles can have similar Voronoi-based volume fractions but drastically different peak drag values depending on the neighbor particles being upstream or downstream. Additionally, even if two particles have an upstream neighbor, the upstream neighbor's precise location will cause either constructive or destructive interference causing a change in peak drag. These aspects of neighbor arrangement will be discussed in Sec. III E.

From the plots in Fig. 11 one can see that particles with the same Voronoi volumes can have significantly different drag. For example, the two red points in Fig. 11(a) have almost the same

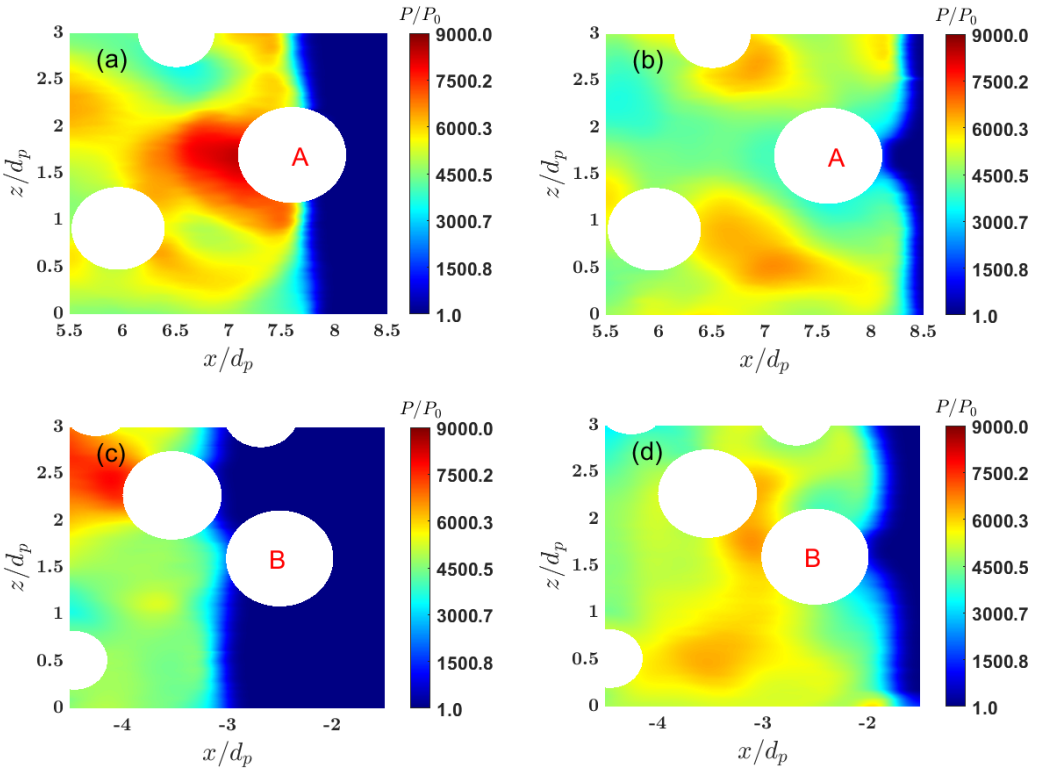

FIG. 12. Plot of normalized pressure (P/P_0) for particle with high peak drag, A, and low peak drag, B. Plots (a) and (c) are when the shock is over the particle, while plots (b) and (d) are when the shock is past the particle.

local volume fraction, but their drag values are dissimilar and of different signs. The particles represented by the red points have C_D peaks of 20.75 and 14.07, respectively. The higher drag particle A experiences a peak force 11.1% higher than the mean value, while the lower drag particle B experiences a peak C_D 24.7% below the mean. The difference in the peak drag is a direct consequence of the position of the neighboring particles and the pressure field. Figure 12 shows the normalized pressure field around the particles at two equivalent times, one when the shock is over the particle and the other after the shock has just passed the particle. Particle A is shown in Figs. 12(a) and 12(b), while the low-drag particle B is shown in Figs. 12(c) and 12(d). The lower drag particle is shielded by an immediate upstream particle that decreases the pressure and thereby decreasing the shock strength impacting the downstream particle. When a particle experiences higher than average drag, it is due to a shock focusing effect caused by the positioning of the upstream particles that increases the local strength of the shock. This result further proves that local Voronoi-based volume fraction is not an adequate measure for predicting the peak drag [29,62]. More exact knowledge of the relative location of the neighbors is crucial in the explanation of high drag versus low drag [67]. As will be discussed below in Sec. III E, to explain the peak drag, it is crucial to characterize the upstream neighbors, and for impulse, one must know about the locations of both upstream and downstream neighbors. In the examinations carried out by Akiki [62] an anisotropic measure of the neighborhood was introduced that involved both upstream and downstream neighbors. However, such a metric was unsuccessful in explaining the peak drag variation in the present problem. The reason being the steady viscous incompressible flow considered by [62] is quite different from the unsteady compressible shock-induced drag being considered here.

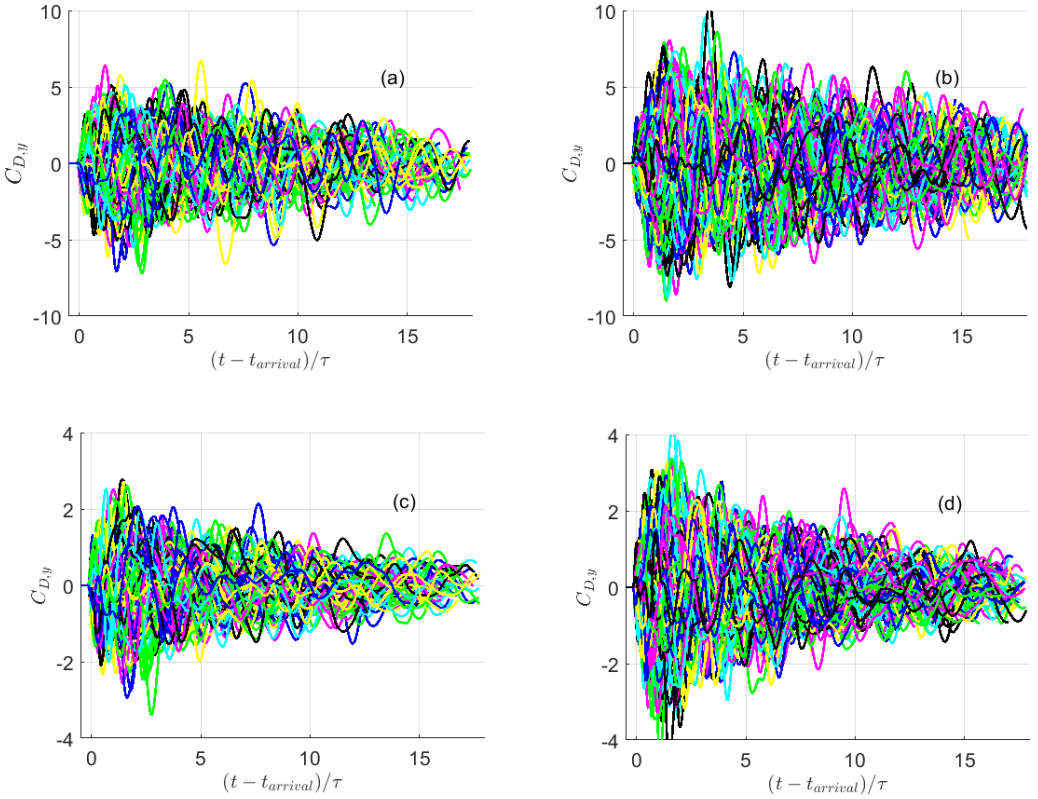

FIG. 13. Plot of $C_{D,y}$, streamwise drag coefficient, as a function of shifted nondimensional time $(t - t_{\text{arrival}})/\tau$. (a) LM10, (b) LM20, (c) HM10, (d) HM20.

C. Transverse force on the particles

The time history of the transverse drag coefficient $C_{D,y}$ experienced by the particles is shown in Fig. 13 for the different cases. $C_{D,z}$ is statistically similar and is not shown. While the transverse drag on an isolated particle would be zero, the perturbations created by neighbor particles within the bed lead to an oscillatory, nonzero drag force on individual particles. Comparing these results with Fig. 6, the peak transverse force can be up to 40% of the peak streamwise force. This can significantly change the particles' motion and lateral dispersion if they can move freely. Part of the lateral force can be interpreted as a drag and not a lift force. Even though the planar incident shock approaches the particle bed propagating along the x direction, once the primary shock enters and travels through the bed, its shape is no longer planar. Its trajectory is not always along the x direction due to the incident shock diffracting off the particles. Thus, the transverse drag occurs when a particle is hit with a nonplanar shock propagating at an angle to the x direction. On the other hand, two side-by-side particles subjected to a planar shock (or even a uniform potential flow) will experience a transverse force, which should be correctly termed lift since the force is perpendicular to the approach flow direction.

The transverse force on the particles fluctuates considerably, with a magnitude that decreases over time. As with the streamwise force, it is of interest to examine if the average transverse force on individual particles is zero over time or if a constant force remains. The y force, when averaged over all the particles within the bed, is expected to be zero, based on results of other research [60]. However, the transverse force could be the same order as the streamwise drag for individual particles. The y impulse of a particle, which is the time integral of the y component of the drag

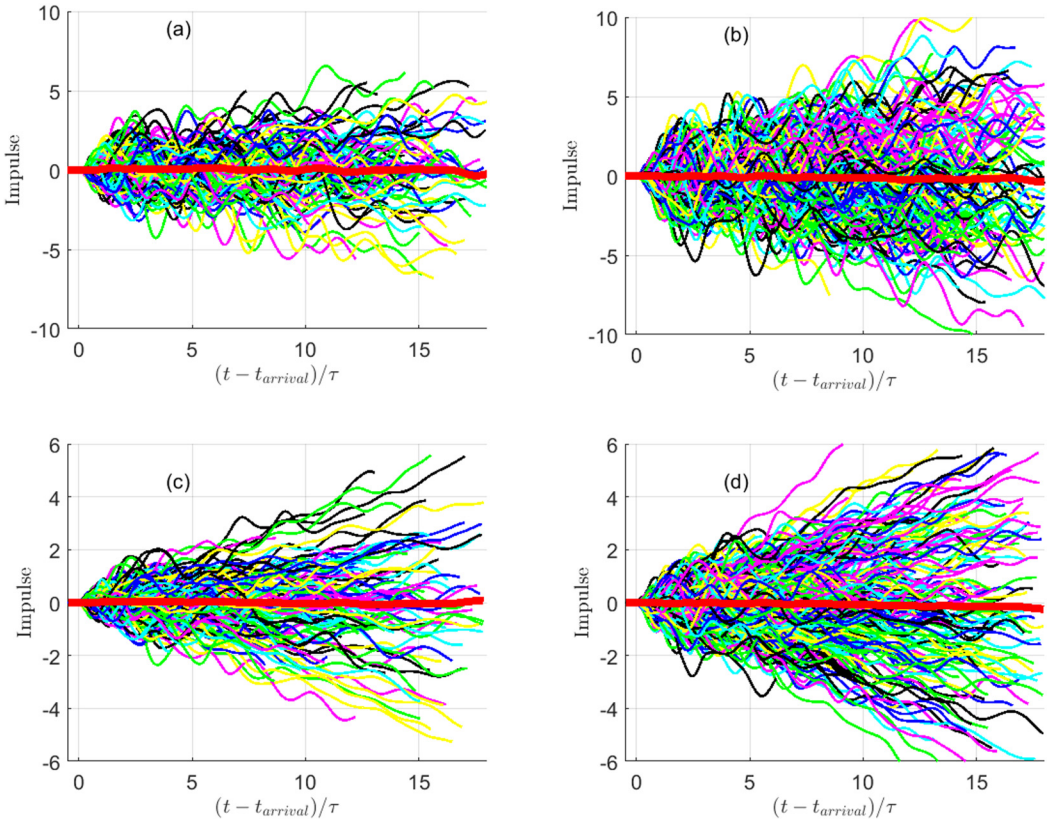

FIG. 14. Plot of impulse in the y direction as a function of shifted nondimensional time $(t - t_{\text{arrival}})/\tau$. (a) LM10, (b) LM20, (c) HM10, (d) HM20.

coefficient, is plotted in Fig. 14 for the four different cases. From the figure, it can be observed that, just like the streamwise force, some particles experience a persistent positive y force, while some others experience a negative y force. The difference is clearly due to the arrangement of neighbors. Plotted as a red line in each subplot is the particle bed average, which is close to a value of zero.

The total transverse force can be further examined using the total transverse force coefficient, defined as $C_{D\perp} = \sqrt{C_{D,y}^2 + C_{D,z}^2}$. The peak total transverse force coefficient is plotted in Fig. 15 for the different particles as a function of streamwise location. Again, shock intensity remains constant as the water shock propagates through the entire bed of particles, in contrast to what was observed in the air-shock simulations of [40]. Particles near the downstream end of the bed experience just as high a transverse force as the front end particles. The magnitude of the transverse force depends only on the neighbor configuration. The average and RMS are presented in Table IV. The average nondimensional force decreases with Mach number, and RMS increases with volume fraction. Figure 16 presents a histogram of the peak $C_{D\perp}$ experienced by the different particles to further

TABLE IV. Average and RMS values for peak streamwise drag.

	LM10	LM20	HM10	HM20
Average	4.33	5.86	1.88	2.44
RMS	1.08	1.31	0.47	0.63

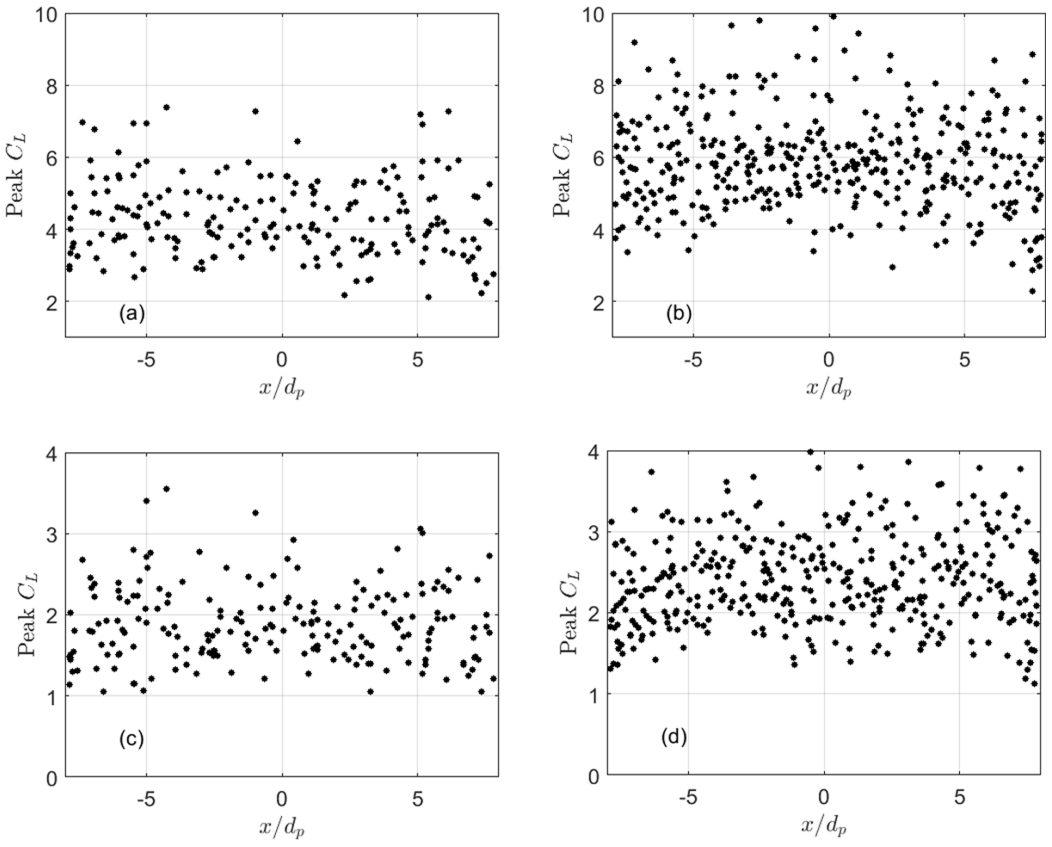

FIG. 15. Plot of normalized peak C_L, total transverse drag coefficient as a function of nondimensional streamwise position x/d_p. (a) LM10, (b) LM20, (c) HM10, (d) HM20.

statistically characterize the transverse force. From its definition, $C_{D\perp}$ is always non-negative. Red lines in the plots represent a log-normal distributions that fit the histogram.

D. Flow fields

For all four cases, a detailed examination of the time history of contours of nondimensional pressure, density, velocity, and local Mach number was carried out. As shown previously in Fig. 8, the shock strength remains constant as it traversed the particle bed, allowing for a simpler statistical analysis needed to interpret the results. Figure 17 shows contour plots of nondimensional pressure for the low Mach number low volume fraction case (LM10). The views are two-dimensional slices in the x-z plane at a fixed transverse location ($y = 0$) through the computational domain. The particles in the simulation are marked using white circles. The circles are different sizes because the plane cuts the particles at different sections in the y direction. Neighboring particles that do not intersect this x-z plane cannot be seen but still greatly impact the flow. The figures show contour plots at seven different times, $t/\tau = 0$, 4, 11.26, 11.32, 12.23, 12.81, and 13.07, to highlight the reflected pressure waves as the incident shock moves through the particle bed. The initial setup is shown in each figure to display the flow properties before any shock-particle interaction occurs. The reflected waves are visible at the early time of $t/\tau = 4$. The pressure fields plotted at the five consecutive time instances clearly illustrate the upstream propagation of the reflections originating at the incident shock front. Constructive or destructive interference forms the complex pressure fields indicated in

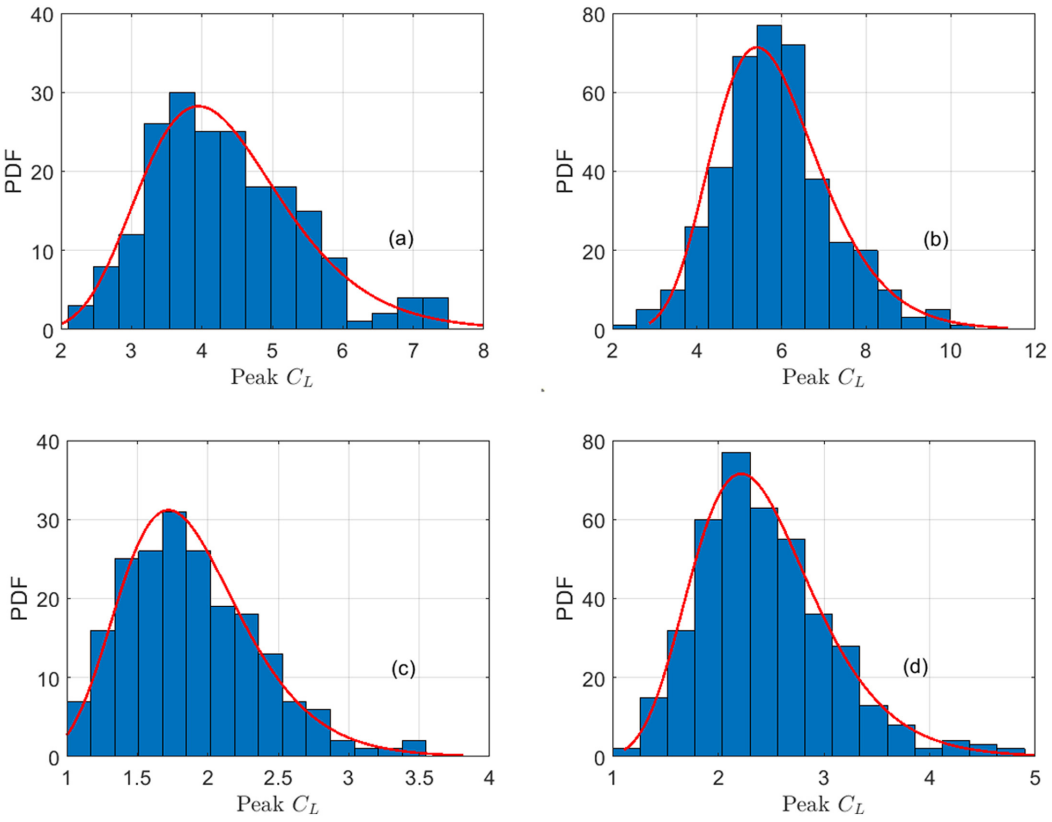

FIG. 16. Histogram plot of peak C_L, total transverse drag. (a) LM10, (b) LM20, (c) HM10, (d) HM20.

the drag histories. As we saw in Figs. 9 and 14, these waves continue to cause drag fluctuations on all the particles. When comparing plots of the same Mach number but different volume fractions (not shown), it is clear that increased volume fraction increases the strength of the reflected waves, which leads to a higher drag force variation in agreement with the results of Table III. As the shock moves farther downstream, the magnitude of the fluctuations imparted by the pressure waves for particles near the front of the bed decreases. Nevertheless, it is interesting to note that there is still a residual persistent positive or negative force that each particle is subjected to when considering the potential flow even as the force fluctuation decays.

Figure 18 shows contour plots of flow Mach number at three different times for two cases: LM10 and HM20. Here the focus is to identify regions of supersonic flow. In the HM20 case, there are regions where the local Mach number is above 1.0; however, these are small and dissipate rapidly. As such, they cause no global decrease in the shock strength. Thus, the flow within the random distribution of particles does not support any shocklet or bow shock formation that would contribute to flow dissipation and nonzero force on the particles. In the HM10 case, localized high Mach number flow areas occur, but they quickly dissipate without impacting the shock strength, similar to HM20. When considering the low Mach cases, the postshock Mach number does not go above 1.0 at any location in the flow. For these cases, there is no mechanism for shock weakening to occur. We also investigated vorticity generated by baroclinic mechanisms within the flow domain. The vorticity is typically generated at the shocklets and standing shocks around the particles, and they contribute to particle force due to their presence in the particle wake as low pressure regions [68,69]. However, these mechanisms are largely absent in the water-shock case due to the subsonic nature of the postshock flow with only small intermittent areas of Mach number above 1.0. It is not

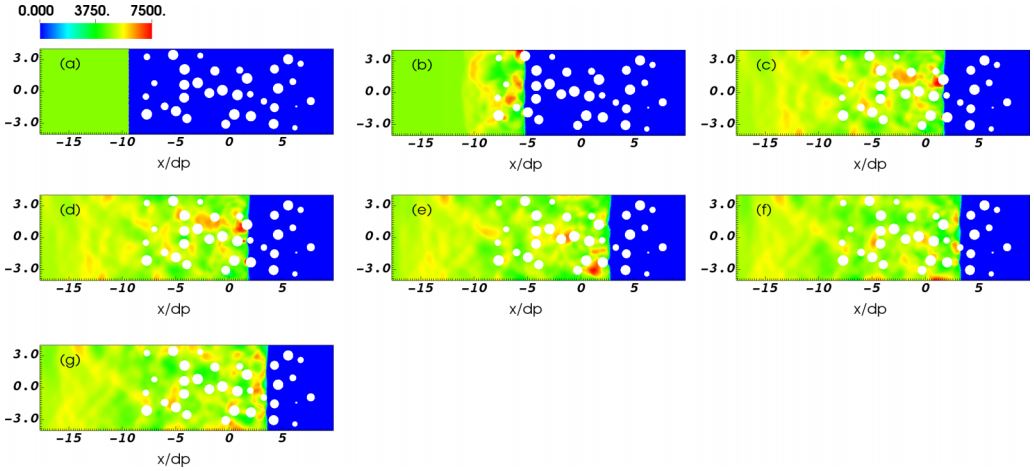

FIG. 17. Contour plots of nondimensional pressure (P/P_0), along the x-z plane at $y = 0$ for $M_s = 1.22$ and $\phi_i = 10\%$ at $t/\tau = 0$, 4, 11.26, 11.32, 12.23, 12.81, and 13.07, $P_0 = 101.3$ kPa.

entirely clear if the postshock flow in water could become supercritical at higher volume fractions and primary shock Mach numbers. If this happens, then associated shocklet-induced dissipation would contribute to the weakening of the primary shock. Also, including viscous effects would significantly cause the shock to weaken as it moves through the bed.

E. Role of neighboring particles

In this section, we examine the role neighbor particles play in determining two key force features: (1) the peak drag force experienced by the particle during shock passage and (2) the persistent increase or decrease of the impulse long after the passage of the shock. First and foremost, it must be stated that we did not observe any correlation between larger (or smaller) than average peak C_D and positive or negative persistent force. In other words, the simulation results showed no correlation between the mechanisms responsible for the higher or lower peak drag and the mechanisms responsible for longer-term positive or negative drag force. Based on this evidence, we will independently ascertain the role of neighbors for the peak C_D and long-term impulse.

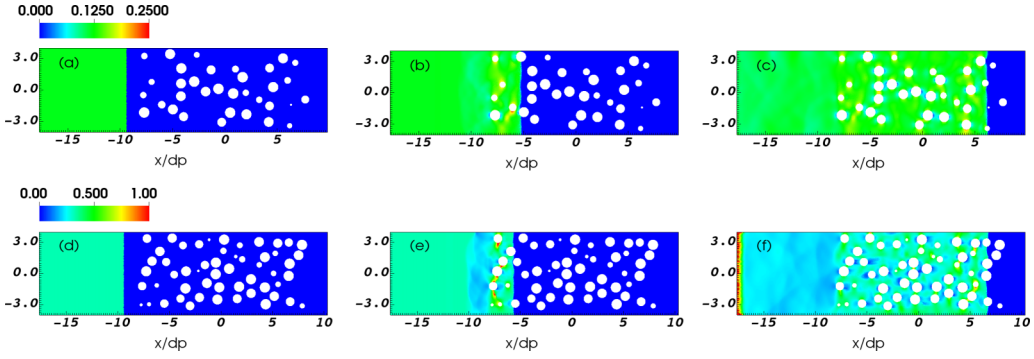

FIG. 18. Top row: Contour plots of Mach number along the x-z plane at $y = 0$ for Mach $= 1.22$ and $\phi_i = 10\%$ at $t/\tau = 0$, 4, and 16 (a–c). Bottom row: Contour plots of Mach number along the x-z plane at $y = 0$ for Mach $= 3.0$ and $\phi_i = 20\%$ at $t/\tau = 0$, 4, and 16 (d–f).

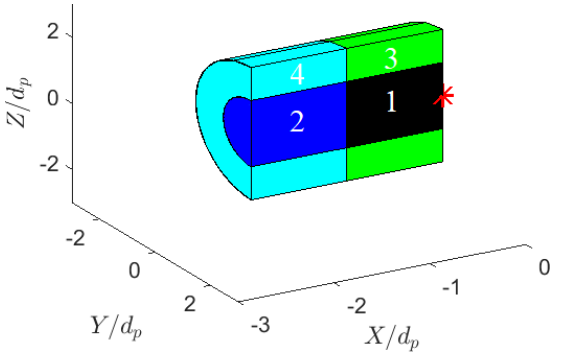

FIG. 19. Half of the upstream region to determine neighbor effects.

As far as the peak drag, the role of the neighboring particles in terms of their relative location can be reasonably argued based on prior investigations. The results of [35] show that even the role of a neighbor located upstream and in line with the particle is somewhat complicated. When the upstream neighbor is sufficiently close, then shielding will occur, decreasing the downstream particle's drag. Contrary to this effect, if upstream particles are close by but located with an offset to the side (i.e., not inline), then a nozzling effect can be expected, resulting in a higher than average drag force. This complex effect was also seen in the case of an FCC array of particles [38]. Thus, in general, for the peak C_D, the upstream neighbors can be expected to have the strongest influence, with virtually no role played by the downstream neighbors. In contrast, both upstream and downstream neighbors become important when considering impulse because both produce wave reflections and potential flow fields. In this section, we attempt to quantify the impact location of neighbors has on an individual particle's drag force.

We start by creating a cylindrical region upstream and downstream of the particle of interest (POI). The cylinder ranges two particle diameters in the streamwise direction and extends radially up to two particle diameters. The upstream section of the cylinder is split into four sections to demarcate those neighbors that are in line versus those that are offset and those that are immediately upstream versus those that are farther upstream. Figure 19 shows half of the cylinder with the four different upstream regions colored. To view the entire upstream cylindrical region, one must mirror the figure across the $y = 0$ plane. In the figure, the flow is moving the positive x direction, and the POI is marked with a red star located at (0,0,0). The dimensions and region numbers are shown in Table V, and there are four identical regions that are downstream of the POI. The following convention will be used for easier description: "Inside" means a particle with its center in the black or blue region, and "Outside" means the particle center is inside the cyan or green region. Note that a particle is considered inside any region only based on its center. Though this is an approximation, it is sufficient for the present qualitative discussion.

The average number of neighbors in each region is computed for each simulation for our investigation. The particles in each simulation were split into three groups based on the peak drag.

TABLE V. Description of regions in cylinder.

Region	Name	Color	Streamwise limits/d_p	Radial limits/d_p
1	Inside 0-d	Black	0-1	0-1
2	Inside d-2d	Blue	1-2	0-1
3	Outside 0-d	Green	0-1	1-2
4	Outside d-2d	Cyan	1-2	1-2

TABLE VI. Average neighbor positions for High, Middle, and Low drag particles.

			Upstream		Downstream	
			Inside 0-2d	Outside 0-2d	Inside 0-2d	Outside 0-2d
M_s 1.22	ϕ 10%	High	0.607	3.75	0.964	4.285
		Middle	0.971	3.336	0.786	3.158
		Low	0.781	2.906	1.281	3.219
M_s 1.22	ϕ 20%	High	1.551	6.414	1.689	6.811
		Middle	1.777	5.964	1.651	5.881
		Low	1.766	6.282	2.188	6.281
M_s 3.0	ϕ 10%	High	0.720	4.16	1.120	3.720
		Middle	0.926	3.162	0.824	3.250
		Low	0.852	3.445	1.037	3.371
M_s 3.0	ϕ 20%	High	1.527	6.272	1.690	6.691
		Middle	1.754	6.021	1.696	5.890
		Low	1.893	6.197	2.036	6.464

The mean and standard deviation were calculated from the peak drag of the different particles. The "High" group was defined as particles with a peak streamwise drag greater than the mean plus one standard deviation. The "Low" group was defined as the particles with a peak drag less than the mean minus one standard deviation. Finally, the "Middle" group consisted of all other particles with peak drag within one standard deviation of the mean. These groups contained enough particles to create a trend when studying the neighbors.

The number of neighbors within each region was calculated for each POI within the High, Low, and Middle groups and then averaged. The resulting average number of neighbors is presented in Table VI for all the cases. In the case of peak C_D, it was unnecessary to distinguish between particles in the region 0 to d and those within d and $2d$ because any particle inline and upstream contributed to shielding effects. The important conclusions to be drawn are (1) more "inside" neighbors directly upstream in the 0 to 2d region contributes to lower peak drag, (2) more "outside" neighbors upstream to the lateral side in the 0 to 2d region contributes to higher peak drag and (3) the peak is not influenced by the downstream particles. In some cases, the Middle group has more neighbors in the 0-2d region than the Low group. Meanwhile, the Middle group has more outside neighbors in 0-2d than the low group. This proves the importance of the combination of the first two factors. Based solely on inline and upstream neighbors, one cannot say if the peak will be higher or low. The neighbors in the outer region must also be considered. Intuitively, one might anticipate this behavior, but we have established their relation from our data set quantitatively. The drag and impulse data are essential for future researchers building analytical models for particle force variations in a particle bed.

A similar analysis of averaging neighbors in the different regions was carried out for the long-term impulse. We considered the mean slope of the impulse towards the end of the simulation to determine the value of the persistent force. Particles that are located towards the downstream end of the bed are discarded from the analysis since they have not sufficiently reached their postshock state of evolution. Again, from the mean and standard deviation of all the particles' persistent force values, the particles were grouped into "High," "Low," and "Middle" bins. Thus, the middle particles experience nearly zero persistent force, while the high and low particles experience positive and negative sustained force. The number of neighbors within each region was calculated for each POI within the High, Low, and Middle groups and then averaged within each group. The resulting average number of neighbors is presented in Table VII for all the cases. The important conclusions to be drawn are (1) Positive persistent force correlates with the presence of more close neighbors in regions 1 and 3 (black and green) upstream and fewer close neighbors downstream (i.e., between 0 and d) downstream. (2) Negative persistent force correlates with the presence of fewer close

TABLE VII. Average neighbor positions for High, Middle, and Low impulse particles.

			Upstream				Downstream			
			Inside 0-d	Inside d-2d	Outside 0-d	Outside d-2d	Inside 0-d	Inside d-2d	Outside 0-d	Outside d-2d
M_s 1.22	ϕ 10%	High	0.727	0.682	1.909	1.636	0.045	0.545	1.227	0.864
		Middle	0.190	0.549	1.706	1.595	0.183	0.686	1.797	1.667
		Low	0.120	1.240	1.680	1.600	0.760	0.520	1.720	1.840
M_s 1.22	ϕ 20%	High	0.750	1.462	3.596	2.981	0.154	0.827	2.615	2.000
		Middle	0.431	1.186	3.275	2.715	0.434	1.390	3.393	2.956
		Low	0.340	1.642	3.132	2.962	0.906	1.132	3.434	2.585
M_s 3.0	ϕ 10%	High	0.714	0.762	2.190	1.667	0.048	0.429	1.286	0.810
		Middle	0.196	0.557	1.690	1.601	0.196	0.690	1.766	1.658
		Low	0.095	1.238	1.524	1.524	0.762	0.571	1.857	1.952
M_s 3.0	ϕ 20%	High	0.796	1.367	3.755	3.163	0.102	0.857	2.633	2.061
		Middle	0.421	1.212	3.238	2.711	0.450	1.389	3.379	2.913
		Low	0.350	1.725	3.200	2.875	0.975	0.975	3.475	2.650

neighbors in regions 1 and 3 upstream and more closer neighbors downstream. (3) Only particles immediately upstream within one diameter seem to influence long-term impulse. In essence, it appears close neighbors contribute to higher pressure, while farther neighbors mean lower pressure, and thus they contribute to persistent positive or negative drag.

1. A simple model

The effect of neighbors in the postshock flow, long after the passage of the shock when the reflected waves are weaker, can be studied with a simple potential flow model. In a potential (inviscid, incompressible) flow, according to D'Alembert's paradox, an isolated object will experience zero drag [59]. In a random bed of particles, the drag on individual particles may be nonzero; however, the sum of all the forces must be zero (i.e., all the particles as a system obey D'Alembert's paradox). This problem was quantitatively explored by Helfinstine, and Dalton [61] for several arrangements of particles. In particular, their calculations for two and three particles in inline arrangements showed the effect of a nearby neighbor to increase the pressure and thereby contribute to positive or negative force depending on the location of the unbalanced neighbor. The closer the particles are to each other, the more significant their potential flow interaction and the impact on the drag force. Neighbors no longer impact a particle's drag once the spacing between particles reaches approximately four particle diameters.

We expect this behavior to remain the same even in low Mach number compressible flows, where the postshock Mach number is subsonic. We performed several simulations for varying structured particle configurations at different subcritical Mach numbers to confirm the inviscid quasisteady effect of neighbors. Here we report the results of only one configuration shown in Fig. 20 as it is

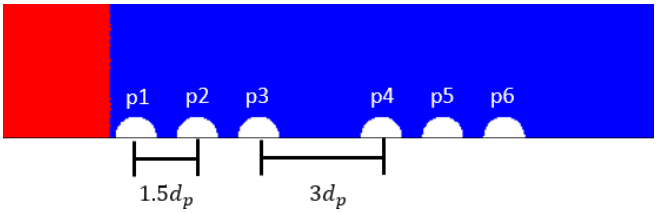

FIG. 20. Structured array of six particles.

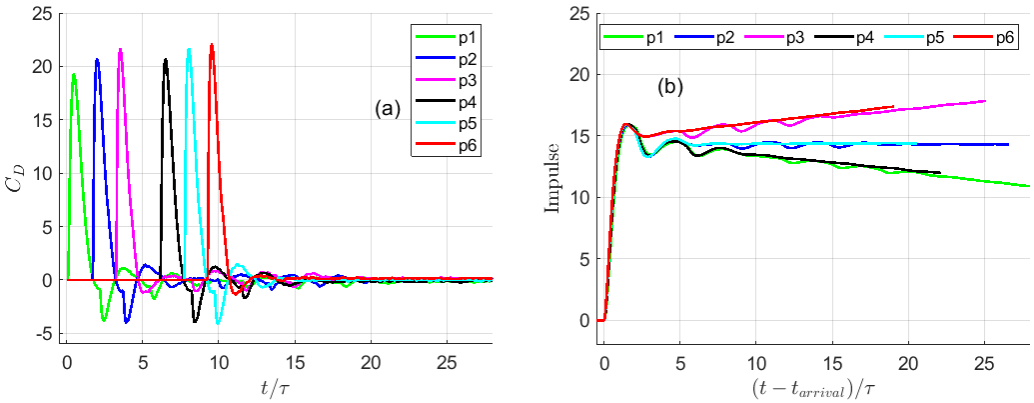

FIG. 21. Plot of drag and impulse for the six particle array.

sufficient to summarize the findings. The structured setup consisted of six inline particles with the flow along the x axis. The particles are spaced at equal distances, except particles 3 and 4 have double the spacing between them. Simulations utilized the axisymmetric nature of the problem to solve the governing equations, where the grid used was created using [70]. Water was used as the working fluid with a Mach 1.22 shock moving over the particles with centers separated by $1.5d_p$. The goal was to determine the drag response of the particles, especially after the shock is well past the particles. The resulting drag and impulse curves are plotted in Fig. 21. The time is nondimensionalized by τ but not shifted by the arrival time in the force graph, Fig. 21(a). Meanwhile, the impulse curves are shifted by the shock arrival time, making it easier to compare the slopes. The drag plot shows an increasing peak between the first three particles, then a decrease for the fourth particle, and an increase towards the sixth particle. The cause for the increased peak is due to shock focusing behind each of the particles. In the random bed configuration, the nearby upstream neighbors are not directly inline, and the presence of other particles contributes to a weakening of constructive interference of diffracted shock. When looking at the impulse, the first and the fourth particle, which are at the front of the three-particle array, have matching impulse with a downward slope, while particles three and six, which have no immediate downstream neighbor, have an upward sloping impulse. Particles 2 and 5 have almost no change in impulse after the passage of the shock. This model problem adequately explains the cause of the sustained positive and negative sloping impulses in the random pack, where the potential flow around an individual particle can be thought of as a superposition of its immediate neighbors.

IV. CONCLUSION

We studied the propagation of an incident shock traversing a random bed of monodispersed particles. Inviscid particle-resolved three-dimensional simulations were completed for four combinations of Mach numbers and particle volume fractions. In this study, we considered the fluid medium to be water, which was modeled using a stiffened equation of state, and compared the results with those reported in [40,41] for air as the fluid medium. We studied the time history of the streamwise and transverse drag forces on each particle along with the corresponding impulses. We concluded from these plots that the average drag and impulse are similar to the isolated particle case. Further, the drag force on the individual particles substantially deviated from the average behavior. This deviation from the average is a direct result of the location of neighbors around a particle. The interactions between particles stem from potential flow pressure fields and reflected waves from neighbors. Most significantly, we observed a sustained drag force on the particles that remains positive or negative even long after the incident shock moves past the particle. As a result, the impulse on the particles continues to slope upwards or downwards

for some particles indicating a long-term quasisteady force. One advantage of investigating this problem with water as the medium is that the postshock flow remains subcritical, and there are no stationary shocklets or bow shocks within the bed after the incident shock has passed through the bed. As a result, there is no energy dissipation within the bed, and the incident shock strength remained the same during the entire simulation period. This allows for more accurate comparison of statistics by averaging along the flow direction. Furthermore, unlike in air, in water the peak drag force on the particles does not decay as the shock travels through the bed. Also, we observed that the peak drag force on the particles do not correlate with the local Voronoi volume fraction, indicating that both the peak as well as the sustained positive or negative impulse are not dependent on the average state of the neighboring particles but on the precise upstream, downstream, or lateral location of the particles. In other words, simple isotropic scalar measures of neighboring particles are not sufficient when attempting to predict the shock-induced particle force.

In addition to the streamwise drag force, the transverse force on the random distribution of particles was also investigated. The average transverse force on the particles was zero since there is no preferred direction perpendicular to the main flow direction. Nevertheless, the transverse force of an individual particle substantially deviated from the average behavior. Again the most striking observation was that the transverse force was persistently pointed in a particular direction (i.e., remained consistently positive or negative along the y and z directions), dependent on the arrangement of neighboring particles. Accordingly, the transverse impulse plots were continuously sloping either positive or negative for all times, even after the shock had moved far downstream. These results clearly illustrate that the transverse force on the particles cannot be neglected in particle motion and dispersion. It must be noted that even though the transverse force is normal to the mean flow direction, part of their origin may still be similar to the drag force. As the incident shock wave and the postshock reflected waves pass over a particle, their direction of propagation is not strictly in the x direction due to their diffraction around the neighboring particles. As a result, each particle within the random pack is subjected to varying local incident flows that contribute to a force along the x direction (drag) and a transverse force.

We also studied the flow field and the features of the incident shock and the reflected waves present in the simulations. The pressure plots showed instances of shielding by an upstream particle contributing to the reduced peak force on a particle, while nozzling effect in the case of others contributing to an enhancement of the peak drag, thus illustrating the importance of arrangement of neighboring particles in determining the positive or negative deviation the peak drag force. The persistent positive and negative force long after the passage of the shock could be explained based on potential flow perturbations around each particle due to its neighbors. Many close upstream (or downstream) neighbors contributed to a long-term positive (or negative) drag force. Another cause of force perturbation in the drag is backward-propagating reflected waves emanating from the interaction of the incident shock with the bed of particles. The diffraction of these reflected waves around the neighbors of each particle dictated its local unsteady pressure distribution, which resulted in variations in the streamwise and transverse drag curves. Since the incident shock maintained its strength due to lack of dissipation, the reflected waves were continually generated at the shock front and contributed to persistent postshock force oscillation on the particles.

Last, an analysis was conducted to examine how neighbor locations influenced the force on a particle. In this analysis, a cylindrical region was considered upstream and downstream of the particle to evaluate the number of particles immediately upstream or downstream of a particle and the number of particles upstream or downstream but located to the lateral side with an offset. Based on correlating the peak drag force of a particle with its upstream or downstream neighbor location statistics, we determined that a higher-than-average peak drag force is the result of nearby upstream neighbors that were located with an offset. While a consistent positive (negative) postshock force is observed to be correlated with the predominant presence of close upstream (downstream) neighbors and fewer downstream (upstream) neighbors.

ACKNOWLEDGMENTS

This work was supported by the Office of Naval Research, under the Naval Undersea Research Program (Contract No. N000141812478). This work was also partly supported in part by the U.S. Department of Energy, National Nuclear Security Administration, Advanced Simulation and Computing Program, as a Cooperative Agreement under the Predictive Science Academic Alliance Program, under Contract No. DE-NA0002378.

[1] A. W. Woods, The fluid dynamics and thermodynamics of eruption columns, Bull. Volcanol. **50**, 169 (1988).
[2] Y. Liu and M. A. F. Kendall, Numerical analysis of gas and micro-particle interactions in a hand-held shock-tube device, Biomed. Microdevices **8**, 341 (2006).
[3] O. Igra and K. Takayama, Shock tube study of the drag coefficient of a sphere in a non-stationary flow, Proc. R. Soc. London A **442**, 231 (1993).
[4] A. Britan, T. Elperin, O. Igra, and J. P. Jiang, Acceleration of a sphere behind planar shock waves, Exp. Fluids **20**, 84 (1995).
[5] H. Tanno, T. Komuro, M. Takahashi, K. Takayama, H. Ojima, and S. Onaya, Unsteady force measurement technique in shock tubes, Rev. Sci. Instrum. **75**, 532 (2004).
[6] H. Tanno, K. Itoh, T. Saito, A. Abe, and K. Takayama, Interaction of a shock with a sphere suspended in a vertical shock tube, Shock Waves **13**, 191 (2003).
[7] M. Sun, T. Saito, K. Takayama, and H. Tanno, Unsteady drag on a sphere by shock wave loading, Shock Waves **14**, 3 (2005).
[8] E. Loth, Compressibility and rarefaction effects on drag of a spherical particle, AIAA J. **46**, 2219 (2008).
[9] M. Parmar, A. Haselbacher, and S. Balachandar, Modeling of the unsteady force for shock-particle interaction, Shock Waves **19**, 317 (2009).
[10] M. Parmar, A. Haselbacher, and S. Balachandar, Generalized Basset-Boussinesq-Oseen Equation for Unsteady Forces on a Sphere in a Compressible Flow, Phys. Rev. Lett. **106**, 084501 (2011).
[11] M. Parmar, A. Haselbacher, and S. Balachandar, Equation of motion for a sphere in non-uniform compressible flows, J. Fluid Mech. **699**, 352 (2012).
[12] S. Annamalai and S. Balachandar, Faxén form of time-domain force on a sphere in unsteady spatially varying viscous compressible flows, J. Fluid Mech. **816**, 381 (2017).
[13] A. V. Fedorov, A. V. Shul'gin, and S. V. Poplavski, Motion of a particle behind the shock wave front, Combust. Explos. Shock Waves **46**, 207 (2010).
[14] Y. Ling, A. Haselbacher, and S. Balachandar, Importance of unsteady contributions to force and heating for particles in compressible flows: Part 1: Modeling and analysis for shock-particle interaction, Int. J. Multiphase Flow **37**, 1026 (2011).
[15] D. L. Frost, Z. Zarei, and F. Zhang, Instability of combustion products interface from detonation of heterogeneous explosives, in *20th International Colloquium on the Dynamics of Explosions and Reactive Systems, Montreal, Canada* (2005).
[16] D. L. Frost, C. Ornthanalai, Z. Zarei, V. Tanguay, and F. Zhang, Particle momentum effects from the detonation of heterogeneous explosives, J. Appl. Phys. **101**, 113529 (2007).
[17] J. L. Wagner, S. J. Beresh, S. P. Kearney, B. O. Pruett, and E. K. Wright, Shock tube investigation of quasi-steady drag in shock-particle interactions, Phys. Fluids **24**, 123301 (2012).
[18] K. T. Hughes, S. Balachandar, A. Diggs, R. Haftka, N. H. Kim, and D. Littrell, Simulation-driven design of experiments examining the large-scale, explosive dispersal of particles, Shock Waves **30**, 32 (2020).
[19] K. Hughes, S. Balachandar, N. H. Kim, C. Park, R. Haftka, A. Diggs, D. M. Littrell, and J. Darr, Forensic uncertainty quantification for experiments on the explosively driven motion of particles, J. Verif. Valid. Uncertain. Quant. **3**, 041004 (2018).
[20] V. Rodriguez, R. Saurel, G. Jourdan, and L. Houas, Impulsive dispersion of a granular layer by a weak blast wave, Shock Waves **27**, 187 (2017).

[21] S. Menon and N. Patel, Subgrid modeling for simulation of spray combustion in large-scale combustors, AIAA J. **44**, 709 (2006).
[22] S. Menon and W. H. Calhoon Jr, Subgrid mixing and molecular transport modeling in a reacting shear layer, in *Symposium (International) on Combustion*, Vol. 26, no. 1 (Elsevier, 1996), pp. 59–66.
[23] Y. Ling, J. L. Wagner, S. J. Beresh, S. P. Kearney, and S. Balachandar, Interaction of a planar shock wave with a dense particle curtain: Modeling and experiments, Phys. Fluids **24**, 113301 (2012).
[24] A. N. Osnes, M. Vartdal, M. G. Omang, and B. A. P. Reif, Computational analysis of shock-induced flow through stationary particle clouds, Int. J. Multiphase Flow **114**, 268 (2019).
[25] A. N. Osnes, M. Vartdal, M. G. Omang, and B. A. P. Reif, Particle-resolved simulations of shock-induced flow through particle clouds at different Reynolds numbers, Phys. Rev. Fluids **5**, 014305 (2020).
[26] T. G. Theofanous, V. Mitkin, and C. H. Chang, Shock dispersal of dilute particle clouds, J. Fluid Mech. **841**, 732 (2018).
[27] R. B. Koneru and S. Balachandar, An assessment of the drag models in the case of a shock interacting with a fixed bed of point particles, J. Fluids Eng. **143**, 011401 (2021).
[28] T. McGrath, J. S. Clair, and S. Balachandar, Modeling compressible multiphase flows with dispersed particles in both dense and dilute regimes, Shock Waves **28**, 533 (2018).
[29] G. Akiki, T. L. Jackson, and S. Balachandar, Pairwise interaction extended point-particle model for a random array of monodisperse spheres, J. Fluid Mech. **813**, 882 (2017).
[30] R. Beetstra, M. A. van der Hoef, and J. A. M. Kuipers, Drag force of intermediate Reynolds number flow past mono-and bidisperse arrays of spheres, AIChE J. **53**, 489 (2007).
[31] S. Tenneti, R. Garg, and S. Subramaniam, Drag law for monodisperse gas-solid systems using particle-resolved direct numerical simulation of flow past fixed assemblies of spheres, Int. J. Multiphase Flow **37**, 1072 (2011).
[32] Y. Y. Tang, E. F. Peters, J. H. Kuipers, S. S. Kriebitzsch, and M. M. van der Hoef, A new drag correlation from fully resolved simulations of flow past monodisperse static arrays of spheres, AIChE J. **61**, 688 (2015).
[33] S. Bogner, S. Mohanty, and U. Rüde, Drag correlation for dilute and moderately dense fluid-particle systems using the lattice Boltzmann method, Int. J. Multiphase Flow **68**, 71 (2015).
[34] A. A. Zaidi, T. Tsuji, and T. Tanaka, A new relation of drag force for high Stokes number monodisperse spheres by direct numerical simulation, Adv. Powder Technol. **25**, 1860 (2014).
[35] P. Sridharan, T. L. Jackson, J. Zhang, and S. Balachandar, Shock interaction with one-dimensional array of particles in air, J. Appl. Phys. **117**, 075902 (2015).
[36] Y. Mehta, T. L. Jackson, J. Zhang, and S. Balachandar, Numerical investigation of shock interaction with one-dimensional transverse array of particles in air, J. Appl. Phys. **119**, 104901 (2016).
[37] Z. Hosseinzadeh-Nik, S. Subramaniam, and J. D. Regele, Investigation and quantification of flow unsteadiness in shock-particle cloud interaction, Int. J. Multiphase Flow **101**, 186 (2018).
[38] Y. Mehta, C. Neal, T. L. Jackson, S. Balachandar, and S. Thakur, Shock interaction with three-dimensional face centered cubic array of particles, Phys. Rev. Fluids **1**, 054202 (2016).
[39] J. D. Regele, J. Rabinovitch, T. Colonius, and G. Blanquart, Unsteady effects in dense, high speed, particle laden flows, Int. J. Multiphase Flow **61**, 1 (2014).
[40] Y. Mehta, C. Neal, K. Salari, T. L. Jackson, S. Balachandar, and S. Thakur, Propagation of a strong shock over a random bed of spherical particles, J. Fluid Mech. **839**, 157 (2018).
[41] Y. Mehta, K. Salari, T. L. Jackson, and S. Balachandar, Effect of Mach number and volume fraction in air-shock interacting with a bed of randomly distributed spherical particles, Phys. Rev. Fluids **4**, 014303 (2019).
[42] S. Annamalai, S. Balachandar, and M. K. Parmar, Mean force on a finite-sized spherical particle due to an acoustic field in a viscous compressible medium, Phys. Rev. E **89**, 053008 (2014).
[43] S. Balachandar and J. K. Eaton, Turbulent dispersed multiphase flow, Annu. Rev. Fluid Mech. **42**, 111 (2010).

[44] C. Lu, S. Sambasivan, A. Kapahi, and H. S. Udaykumar, Multi-scale modeling of shock interaction with a cloud of particles using an artificial neural network for model representation, Procedia IUTAM **3**, 25 (2012).
[45] P. Das, O. Sen, K. K. Choi, G. Jacobs, and H. S. Udaykumar, Strategies for efficient machine learning of surrogate drag models from three-dimensional mesoscale computations of shocked particulate flows, Int. J. Multiphase Flow **108**, 51 (2018).
[46] J. Behrendt, S. Balachandar, J. Garno, and T. P. McGrath, Modeling of shock-induced force on an isolated particle in water and air, Phys. Fluids **34**, 016108 (2022).
[47] J. Zhang, T. L. Jackson, and A. M. D. Jost, Effects of air chemistry and stiffened EOS of air in numerical simulations of bubble collapse in water, Phys. Rev. Fluids **2**, 053603 (2017).
[48] P. N. Sun, D. Le Touzé, G. Oger, and A. M. Zhang, An accurate SPH Volume Adaptive Scheme for modeling strongcompressible multiphase flows. Part 1: Numerical scheme and validations with basic 1D and 2D benchmarks, J. Comput. Phys. **426**, 109937 (2021).
[49] R. Saurel and R. Abgrall, A simple method for compressible multifluid flows, SIAM J. Sci. Comput. **21**, 1115 (1999).
[50] M. S. Liou, A sequel to AUSM: AUSM+, J. Comput. Phys. **129**, 364 (1996).
[51] A. Haselbacher, A WENO reconstruction algorithm for unstructured grids based on explicit stencil construction, in *43rd AIAA Aerospace Sciences Meeting and Exhibit* (2005), p. 879.
[52] Y. Ling, A. Haselbacher, and S. Balachandar, Transient phenomena in one-dimensional compressible gas-particle flows, Shock Waves **19**, 67 (2009).
[53] Y. Mehta, T. L. Jackson, and S. Balachandar, Pseudo-turbulence in inviscid simulations of shock interacting with a bed of randomly distributed particles, Shock Waves **30**, 49 (2020).
[54] P. Das, O. Sen, G. Jacobs, and H. S. Udaykumar, A sharp interface Cartesian grid method for viscous simulation of shocked particle-laden flows, Int. J. Comput. Fluid Dyn. **31**, 269 (2017).
[55] Y. Ling, A. Haselbacher, S. Balachandar, F. M. Najjar, and D. S. Stewart, Shock interaction with a deformable particle: Direct numerical simulation and point-particle modeling, J. Appl. Phys. **113**, 013504 (2013).
[56] P. O. Persson and G. Strang, A simple mesh generator in MATLAB, SIAM Rev. **46**, 329 (2004).
[57] H. Si, TetGen, a Delaunay-based quality tetrahedral mesh generator, ACM Trans. Math. Softw. **41**, 1 (2015).
[58] S. Honghui and K. Yamamura, The interaction between shock waves and solid spheres arrays in a shock tube, Acta Mech. Sinica **20**, 219 (2004).
[59] J. le Rond d'Alembert, Theoria resistentiae quam patitur corpus in fluido motum, ex principiis omnino novis et simplissimus deducta, habita ratione tum velocitatis, figurae, et massae corporis moti, tum densitatis compressionis partium fluidi, Berlin-Brandenburgische Akademie der Wissenschaften, Akademie-Archiv call number I-M478 (1749).
[60] W. Xiao, C. Mao, T. Jin, K. Luo, and J. Fan, Fully resolved simulation of a shockwave interacting with randomly clustered particles via a ghost-cell immersed boundary method, Phys. Fluids **32**, 066105 (2020).
[61] R. A. Helfinstine and C. Dalton, Unsteady potential flow past a group of spheres, Comput. Fluids **2**, 99 (1974).
[62] G. Akiki, T. L. Jackson, and S. Balachandar, Force variation within arrays of monodisperse spherical particles, Phys. Rev. Fluids **1**, 044202 (2016).
[63] M. G. Pai and S. Subramaniam, Modeling droplet dispersion and interphase turbulent kinetic energy transfer using a new dual-timescale Langevin model, Int. J. Multiphase Flow **33**, 252 (2007).
[64] K. Yazdchi, S. Srivastava, and S. Luding, Micro-macro relations for flow through random arrays of cylinders, Composites Part A **43**, 2007 (2012).
[65] Y. Matsumura and T. L. Jackson, Numerical simulation of fluid flow through random packs of polydisperse cylinders, Phys. Fluids **26**, 123302 (2014).
[66] J. Quintanilla and S. Torquato, Local volume fraction fluctuations in random media, J. Chem. Phys. **106**, 2741 (1997).

[67] V. M. Boiko, K. V. Klinkov, and S. V. Poplavskii, Collective bow shock ahead of a transverse system of spheres in a supersonic flow behind a moving shock wave, Fluid Dyn. **39**, 330 (2004).

[68] K. Fujisawa, T. L. Jackson, and S. Balachandar, Influence of baroclinic vorticity production on unsteady drag coefficient in shock-particle interaction, J. Appl. Phys. **125**, 084901 (2019).

[69] G. S. Shallcross, R. O. Fox, and J. Capecelatro, A volume-filtered description of compressible particle-laden flows, Int. J. Multiphase Flow **122**, 103138 (2020).

[70] J. R. Shewchuk, Triangle: Engineering a 2D quality mesh generator and Delaunay triangulator, in *Workshop on Applied Computational Geometry* (Springer, Berlin, 1996), pp. 203–222.